

Modeling of a Semi-Active Flapping Foil Power Generator (FFPG) using Deep Learning

Research Project - Master of Aerospace Engineering

Authors:

BATAILLIE Paul

paul.bataillie@student.isae-supero.fr

STOICA Andrei-Dan

andrei-dan.stoica@student.isae-supero.fr

Tutors:

GOWREE Erwin R.

erwin-ricky.gowree@isae-supero.fr

BAUERHEIM Michael

michael.bauerheim@isae-supero.fr

Contents

| | | |
|-----------|---|-----------|
| 1 | Declaration of Authenticity | 1 |
| 2 | Contributions | 1 |
| 3 | Abstract | 2 |
| 4 | Introduction | 4 |
| 5 | State of the Art | 6 |
| 5.1 | Fully Activated Motions | 6 |
| 5.2 | Semi-Active System | 7 |
| 5.3 | Physics and Theory regarding the Operating Regimes | 9 |
| 6 | Power Extraction Efficiency | 12 |
| 7 | Aerodynamics of a Flapping Airfoil Power Generator | 13 |
| 7.1 | Pitch and Plunge Airfoil | 13 |
| 7.2 | LESP Discrete Vortex Method (LDVM) | 13 |
| 7.2.1 | Theory | 13 |
| 7.2.2 | Implementation | 14 |
| 7.2.3 | Validation | 15 |
| 7.3 | Unsteady Aerodynamic Model using Deep Learning | 19 |
| 7.3.1 | Multilayer Perceptron Architecture (MLP) and Inputs | 19 |
| 7.3.2 | Training and Validation | 20 |
| 7.3.3 | Performance Metric | 21 |
| 7.4 | Parametric Analysis and Single-Objective Optimization | 21 |
| 7.4.1 | Parametric Analysis | 22 |
| 7.4.2 | Problem Formulation | 23 |
| 7.4.3 | Optimization using Genetic Algorithm | 23 |
| 8 | Aeroelastic Modeling of a Flapping Foil Power Generator | 24 |
| 8.1 | Structural Model | 24 |
| 8.1.1 | System Properties | 24 |
| 8.1.2 | Governing equations | 25 |
| 8.2 | Control Strategy | 26 |
| 8.3 | Coupling between Structural and Aerodynamical Models | 27 |
| 8.4 | Active Learning | 28 |
| 8.5 | Parametric Analysis | 29 |
| 8.6 | Multi-Objectives Optimization | 32 |
| 9 | Analysis of the Optimal Flapping Foil Power Generator | 35 |
| 10 | Conclusion and Perspectives | 40 |

1 Declaration of Authenticity

The authors certify that this assignment is entirely their own work. Quotations from literature are properly indicated with appropriated references in the text. All literature used in this piece of work is indicated in the bibliography placed at the end. The authors confirm that no sources have been used other than those stated.

The authors understand that plagiarism (copy without mentioning the reference) is a serious examinations offence that may result in disciplinary action being taken.

Date: March 27, 2025

Signatures



2 Contributions

This section aims at clarifying the contribution of the authors in this work. This clarification was asked by the tutors of this research project.

STOICA Andrei:

- Section 4 - **Introduction**
- Section 5 - **State of the Art** and its subsections 5.1, 5.2, 5.3
- Section 6 - **Power Extraction Efficiency**
- Sub-Subsection 7.2.3

BATAILLIE Paul:

- Section 6 - **Power Extraction Efficiency**
- Section 7 - **Aerodynamics of a Flapping Airfoil Power Generator** and its subsections 7.1, 7.2, 7.3, 7.4
- Section 8 - **Aeroelastic Modeling of a Flapping Foil Power Generator** and its subsections 8.1, 8.2, 8.3, 8.4, 8.5, 8.6
- Section 9 - **Analysis of the Optimal Flapping Foil Power Generator**

3 Abstract

Flapping foils are well known for their potential of harvesting energy. One practical way is to recover the energy from the heaving motion through a semi-activated foil for which the pitching motion is prescribed. This paper develops a more realistic representation of such system by modeling the aeroelasticity of a Flapping Foil Power Generator (FFPG) using Deep Learning. Given the advantage of leading edge vortex for increasing the performance, LESP Discrete Vortex Method is found to be a suitable model for predicting the aerodynamic loads acting on the foil. The coupling between the structure and the aerodynamic model is performed with a Feedforward Neural Network (FNN). An Active Learning procedure ensures the convergence on the modeling of the fluid-structure interaction. A multi-objective optimization conducted with a genetic algorithm (NSGA2) allowed to identify the primary parameters driving such system, namely the reduced frequency k , the stiffness K_h and the pitching amplitude θ_0 . This study demonstrates that both the aerodynamical effects associated to dynamic stall and the natural excitation of the system must be exploited to optimize the efficiency of such FFPG. A simple relation is derived to optimize the reduced frequency to take advantage of the leading edge vortex that is developing on the foil undergoing significantly large pitching amplitudes. The implementation related to this work is publicly available on GitLab.

Nomenclature

| | |
|-----------------------|--|
| α_{eff} | Effective Angle of Attack (rad) |
| Δt | Time Step (s) |
| η | Aeroelastic Efficiency |
| η_{aero} | Aerodynamic Efficiency |
| ω | Angular Frequency (rad.s^{-1}) |
| ρ | Density (kg.m^{-3}) |
| θ | Pitching Motion (rad) |
| θ_0 | Pitching Amplitude (rad) |
| b | Semi-chord (m) |
| c | Chord (m) |
| C_h | Damping per meter span (N.s.m^{-2}) |
| C_L | Lift Coefficient (—) |
| C_M | Pitching Moment Coefficient on the rotational axis (—) |
| C_P | Coefficient of Power (—) |
| f | Frequency (Hz) |
| h | Position on the Heaving axis (m) |
| h_0 | Heaving Amplitude (m) |
| I_θ | Moment of Inertia per meter span (kg.m) |
| k | Reduced Frequency based on angular frequency ω and semi-chord b |
| K_h | Stiffness per meter span (N.m^{-2}) |
| L | Total Lift Force (N) |
| LESP | Leading Edge Suction Parameter (—) |
| m | Mass of the FFPG per meter span (kg.m^{-1}) |

| | |
|----------------------|---|
| M_θ | Pitching Moment (N.m) |
| M_{control} | Moment imposed by the controller on the pitching axis (N.m) |
| P_c | Power consumed by the controller per meter span (W.m^{-1}) |
| P_e | Power extracted per meter span (W.m^{-1}) |
| Re | Reynolds Number based on the chord ($-$) |
| T | Period (s) |
| t | Time (s) |
| U_∞ | Freestream Velocity (m.s^{-1}) |
| U_c | Convection Velocity (m.s^{-1}) |
| x_f | Location of the rotational axis |

4 Introduction

Extensive research has been done in recent decades for developing alternative power generation systems using renewable sources, such as wind [1] or hydraulic energy [2]. Particularly, recent attention has been accorded to the potential of harnessing flow energy through a heaving and pitching foil. This is proven by the great variety of documented research on both theoretical and experimental studies of flapping motion.

The earliest scientific theories concerning flapping wing motion are related to heaving an airfoil in an uniform flow. Thus, by performing independent studies in 1909, respectively in 1912, Knoller [3] and Betz [4] observed that plunging a wing in a free stream flow induces an effective angle of attack and a resultant force composed of both lift and thrust components. This phenomenon is nowadays known as Knoller-Betz effect. Later in 1922, Katzmayer [5] validated experimentally this observed effect, but in a relative way. Thus, instead of heaving the airfoil, Katzmayer sinusoidally oscillated the freestream velocity. His measurements concluded that an airfoil mounted in an oscillating wind stream experienced a thrust force.

When it comes to the coupling between a pitching and a plunging motion, this behavior of oscillating foils is reminiscent of biological structures such as insect wings or fish body's which have developed mechanisms to propel themselves efficiently relying upon unsteady flow-body interactions [6].

Additionally to their application as propellers, flapping foils are also capable of harvesting energy from uniform streams, vortical structures and, of course, tidal energy. Firstly, the capacity of a foil to absorb the energy of the incoming flow is clearly demonstrated in flow-induced vibrations such as flutter which became a frequent phenomenon during World War I and in the interwar period [7]. Since this phenomenon represent a great threat for the safety operation of any aircraft, unsteady aerodynamics theory became more and more important for the investigation of flutter. Therefore, given the deficiency of a quasi-steady approximation for the flow around an oscillating airfoil, namely the neglected effect of the wake on the flow around the airfoil, Theodorsen [8] suggested an analytical method in 1934 which depicts the unsteady lift and moments on a pitching and plunging thin flat plate equipped with a flap. As an extension of Theodorsen's work, Garrick [9] modelled the streamwise force, thus the propelling or the drag force associated to a pitching-plunging airfoil based on Theodorsen's equations.

Along with the studies aforementioned that are only tangentially linked to the extraction of energy via a pitching-plunging airfoil, a breaking through study in this area represents the so called 'wingmill' pioneered by McKinney and DeLaurier (1981) [10]. Interestingly, their research encompasses both a theoretical study and an experimental assessment for such system in which both pitching and plunging motions are assumed to be sinusoidal. In their study, the harmonically oscillating wing that was able to extract wind flow energy achieved a surprising efficiency comparable to a rotary design, more precisely 28.3% [10]. For further highlighting the potential of such system, we recall here the theoretical upper limit efficiency of a steady wind turbine which is 59.3%, commonly known as Betz limit [4], [11].

Since then, related studies regarding this manner of producing energy was investigated by numerous researchers, such as K.D. Jones, K. Lindsey and M.F. Platzer [12] (1997), T. Kinsey and G. Dumas (2008) [13], Zhu and Peng (2009) [14], Xiao and Liao (2012) [15].

Several ways of improvements of such mechanisms have been examined. A first one concerns an optimized combination of motion parameters (reduced frequency f^* , maximum effective AOA α_{eff} and heaving amplitude h), as well as geometrical parameters (pivot location, foil profile) for maximizing the harvest of energy. This approach is similar to the parametric study performed by Kinsey and Dumas [13] for sinusoidal motions or the one by Xiao and Liao [15] in which they consider a non-sinusoidal heaving by conserving the same phase shift of $\Delta\phi = 90^\circ$ between the two motions as for the former study.

Nevertheless, one can observe here that both the pitching and the plunging motions are fully constrained and imposed without considering the power required by the external actuators to enable the considered motions. That being so, these studies are concentrated on the hydrodynamic heaving and pitching power by assuming the desired motions and therefore by decoupling the interaction between oscillating system and the surrounding fluid.

Given the two degrees of freedom of such devices, three possibilities are theoretically available, namely: fully activated, semi-passive, and fully passive foils. Regarding the fully active foil, both motions are forced given a full control strategy. Despite its high aerodynamic efficiency [13],[15], its deficiency is related to the fact that it cannot be easily integrated with any power take-off (PTO) system [16].

For the semi-passive system, the movement of one degree of freedom is prescribed as a periodic motion (e.g., pitching) and the power is extracted from the other movement (e.g., plunging), part of it being used to drive the pitch motor. It is worth noting that this type of system takes advantage of the fluid-structure interaction for extracting energy by the fact that the prescribed periodic motions produces periodic variations in the lift and drag forces. Consequently, the time-varying forces and moments trigger in their turn the motion on the heaving axis. Due to the rather straight forward implementation, this type of mechanisms was analyzed experimentally as a prototype by Zhen Liu [17]. Additionally, theoretical studies were performed by using a fluid-structure interaction model, as per the study of Zhu and Peng in 2009 [14] or the study of Javed in 2018 [18].

Lastly, the fully passive configuration is the one in which the foil moves entirely under the influence of fluid forces without any external activation. For this system, the coupling pitch-plunge motion is determined directly by a fluid-structure interaction problem. By having a numerical approach in which the airfoil is mounted on a damper and a rotational spring, Peng and Zhu (2009) highlight the importance of well designing the system. They showed that the system undergoes four distinct behaviours depending mostly on the rotational axis and on the rotational spring stiffness, only one being favorable for power extraction [19]. Additionally, Boudreau (2018) demonstrated experimentally that the position of the pitch axis is a crucial parameter for the divergence instability [20]. This study also illustrates the feasibility of such system over a large space of parameters.

Flapping foils can undergo two regimes: propulsion and power extraction. Therefore, the fundamental difference between these two regimes needs to be well established for a numerical analysis. Considering this, this paper begins with scrutinizing the general knowledge linked to this field, followed by a description of the two regimes. The definitions of the efficiencies considered in this work will be provided.

The present study proposes to develop an aeroelastic model of a semi-activated Flapping Foil Power Generator (FFPG) using Deep Learning. This work will be split into three parts.

Firstly, the motivation of using the LESP Discrete Vortex Method for the predictions of the aerodynamic loads on the foil will be provided. After performing a validation of the aforementioned method, a neural network will be trained to replicate, with some generalization capabilities, the outputs of LDVM. The reason of using a neural network is to allow the coupling between the aerodynamical and structural models. Further discussion will be performed but LDVM (in its current form) cannot be coupled directly with a structural model because of some implementation issues.

Secondly, a simple structural model is developed using the Lagrange's formulation. Only then, a coupling between the aerodynamical model (neural network) and the structural model is possible. Since a semi-activated flapping foil is investigated, the pitching motion will be prescribed by using a PID controller and the heaving motion will result from the fluid-structure interaction. Moreover, once introducing the passive heaving motion into play, the motion of the system will no longer be similar to what has been prescribed when the neural network was trained. Thus, an active learning procedure will ensure convergence on an aeroelastic model in line with LDVM predictions.

Finally, a multi-objective optimization conducted with a genetic algorithm (NSGA2) will be conducted in order to assess the best design for a Flapping Foil Power Generator. A discussion will be conducted on how the aerodynamics and the structure affects such system based on the visualization of the leading and trailing edge vortexes developing on the foil.

5 State of the Art

5.1 Fully Activated Motions

The idea of energy extraction through an oscillating airfoil was put in place by the pioneering study of McKinney and DeLaurier back in 1981. They were the first to conduct a comprehensive investigation of an oscillating foil windmill intituled the 'wingmill' which harnessed energy from a steady flow. As illustrated in Figure 1, the wing exhibited a fully activated heaving and pitching motions, using a Scotch-yoke mechanism that translates the heaving motion into a horizontal rotary shaft motion. This shaft is also connected to the pitch control cable so that the pitching and plunging motions are coupled by the desired phase [10].



Figure 1: Experimental Setup [10]

In their study, they analysed the power extraction regime both theoretically and experimentally by means of a friction brake measuring the torque on the horizontal shaft. It was observed that the average power extracted per cycle reached its maximum value for a phase shift between the pitching and the heaving motion $\phi = 110^\circ$, while efficiency had a maximal value for a phase of 90° [10].

Additionally, their work identifies the most relevant parameters for power production, namely reduced frequency, pitch amplitude, phase angle between pitching and plunging sinusoidal motions, and the ratio between the heaving amplitude and the chord. This shows that the most important parameters are the ones that play a role in the kinematics while the geometrical parameters have a secondary effect. This is an important statement for potentially conducting an optimization of the power extraction by such devices, as it is further shown in this study.

Based on the knowledge of the possibility of power extraction throughout simultaneously heaving and pitching foils, T. Kinsey and G. Dumas performed a parametric study by investigating its theoretical performance (its produced power and efficiency) through CFD simulations [13] at a Reynolds number of $Re = 1100$. The simulations were done for a NACA 0015 using the commercial CFD code FLUENT and the flow was considered 2D, laminar and unsteady. Their work implied mapping the required correlation between the pitching amplitude θ_0 and the reduced frequency f^* such that the motion may be representative either of power extraction or propulsion. The associated graph is shown in Figure 2, the theory and the physics that qualitatively enable predicting one regime or the other being later presented in subsection 5.3.

Lastly, it is worth mentioning that the parametric study done by Kinsey and Dumas was performed by keeping the heaving amplitude $h_0 = c$, the pitching rotation axis $x_f = c/3$ and all other parameters constant and by varying only the frequency and the pitching amplitude. For this case, the resulted efficiency peaked at 34% for a relatively high pitching amplitude $\theta_0 \approx 75^\circ$ and reduced frequency $f^* \approx 0.15$, corresponding to a maximum effective angle of attack over one cycle of about 35° at which dynamic stall occurs [13].

A similar and quite complementary investigation was done by Manuel Garcia Lucas in 2022 in which he investigated the power extraction performances of a pitching-plunging airfoil in turbulent conditions ($Re = 5 \times 10^5$) through unsteady CFD simulations [21]. His research showed that the turbulent condition could provide a much higher power coefficient (21.5% more) and efficiency (16.4% higher) than compared

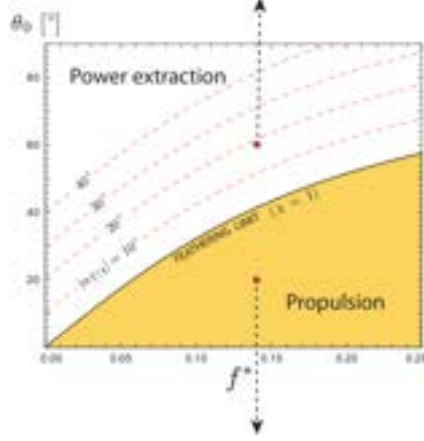


Figure 2: Operating regime as a function of (f^*, θ_0) [13]

to laminar flow conditions. Nevertheless, the parameters corresponding to the best performing case are very close to the ones found by Kinsey and Dumas [13], namely $f^* = 0.15$ and $\theta_0 = 75^\circ$.

Despite the fact that the sinusoidal function may represent the most intuitive periodic differential function, it is interesting to assess whether a different type of periodic function may improve the maximum extracted energy per cycle or the efficiency. Thus, after examining which of pitching or plunging had the potential to bring more improvements, Xiao et al. [15] performed a detailed numerical investigation of the trajectory impact of a specially designed trapezoidal-like pitching motion and a sinusoidal plunging motion on the power harvesting performance. Moreover, the two motions were always shifted by $\phi = 90^\circ$, the pitch trajectory being adjustable by means of a parameter β from a sinusoid $\beta = 1$ to a square function $\beta = +\infty$.

Therefore, by using a NACA0012 airfoil at a moderate Reynolds number $Re = 10^4$ and ranging β from 1 to 4, it was shown that depending on the value of β , the performance exhibited a non-linear trend. When performing one to one comparisons with the sinusoidal motions, the maximal efficiency was demonstrated to increase as high as 50% over the $\beta = 1$ case by adopting $\beta = 1.5$. Moreover, similar improvements were displayed for $\beta = 1.25$. On the other hand, a maximum of 48% decrease of efficiency was observed for $\beta = 4$ compared to the same sinusoidal setup. The authors stress here that the root cause for this trend is the fact that for β slightly larger than unity, the consumed energy related to the pitching moment is smaller than the positive energy thanks to heaving. However, with β becoming far larger than 1, namely for very sharp rotations, the opposite behaviour occurs. This being the case, an optimum beta around 1.5 has demonstrated the best performance over a wide range of Strouhal numbers for the kinematic parameters studied.

5.2 Semi-Active System

Since one of the goal of this study is finding the combination of optimum parameters for a semi-active pitching-plunging system for energy harvesting, a distinctive emphasis is placed to the research in this field. The authors recall here that while for the fully activated system the attention is put mostly on the operational parameters, its performance being related to the aerodynamical loading, the semi-active system relies on a fluid-structure interaction problem. Thus, in order to properly predict the amount or recoverable energy for this type of system, it is crucial to resolve the coupling between the aerodynamic forces at each instance in time as well as the structural dynamics and response of the device.

Therefore, Zhu and Peng [14] numerically investigated the performance of such an apparatus at low Re by a numerical method based on the Navier-Stokes equations. In their study, the airfoil is mounted on a damper with a constant damping factor c , the viscous damper being responsible for the extraction of energy. The foil is able to pitch thanks to an imposed sinusoidal motion, while the heaving motion is generated from the coupling. The authors underline a couple of employed assumptions that may affect the results: the consumed power for ensuring the sinusoidal pitching trajectory relies only on the aerodynamic pitching moment, the rotational moment of inertia around the pitching axis being assumed to be negligible by comparison with the added mass effect. Therefore, the power needed for pitching is simply $P_{M\theta}(t) = M_{aero}(t)\dot{\alpha}$. Additionally, a similar assumption is made when it comes to the equation

of motion for heaving, the inertia of the airfoil being neglected. Thus, the equation of translation for the foil is written as $\dot{c}h(t) = F_y(t)$.

Passing to the most important results of the study, the analysis show that both the net power extraction and the efficiency η peak for a position of the axis of rotation $x_p \approx 0.3 - 0.4c$. It was also found that this behaviour is attributed mostly to the reduction in the mean power needed for pitching the foil, the suction peak being located closer to the leading edge throughout half of a period [14].

Additionally, it was shown that the heaving amplitude h_0 increases as the frequency decrease, such that there is not a clear relationship between the heaving velocity and the frequency. Nevertheless, the magnitude of the power extracted varies with the square of the vertical velocity. That's the reason why a trend regarding the net power output as a function of frequency is not straight forward.

Finally, it was shown that the net power is increasing as the pitching amplitude θ_0 rises. Moreover, leading edge vortex (LEV) was found to be a key factor for energy recovery. Particular conditions are needed for this event to occur. Since the LEV is associated to a region of low pressure, if the location of LEV is synchronised with the pitching motion such that it is located as far as possible from the pitching axis (ideally at the trailing edge) and generates a moment in the same direction as the pitching moment, this would enable energy transfer from the flow field to the system.

Furthermore, an additional study that includes Re and a translational spring effect is the one performed by Javed et al. in 2018 [18]. In their study, the performance of a semi-active pitching and plunging NACA0015 foil is explored at Reynolds numbers ranging from 5000 to 50000. As per the previous exemplified study, a sinusoidal pitching motion is prescribed and energy is extracted from the translational motion. Nevertheless, the unitary span wing is mounted on a damper and a spring, the equation for the translational motion is now: $m\ddot{y} + b\dot{y} + ky = F_y(t)$. However, the power associated to both modes is calculated as presented by Kinsey and Dumas [13] (a more in depth presentation on how the power and the efficiency could be computed for the power extraction regime and depending on the considered approach respectively is performed in section 6). Also, all the parameters were non-dimensionalized.

Regarding the effect of the spring on the device, this study showed that aerodynamic force and moment coefficients increase with increasing stiffness values. The presence of the spring also affects the heaving amplitude by minimizing it as the spring gets stiffer. Additionally, it was observed that the net coefficient of power and the heaving amplitudes tend to go up by increasing Reynolds numbers.

Finally, one notable related study is the numerical and experimental research performed by Zhen Liu et al. [17] in which experiments were conducted in a water channel for a NACA0020 foil at $Re = 48,000$. Similar to the previous numerical studies, the energy is recovered by means of a damper. Contrary to the numerical linear (viscous) damper typically employed in the numerical analysis, this study employs a magnetic damper and an electric generator that provide a constant load (invariant to the rotational speed) and a varying load (which was found to be a quadratic function of the angular velocity), respectively as figured in 3. The authors point out here that five magnetic dampers with damping factors ranging from 0.5 to 2.5 were tested together with 3 monotonically increasing resistance of the generator (for the varying loading cases).

On top of explaining the most relevant outcomes of this study, it is worth showing the particularities of the experimental test rig, the mathematical modelling of the dynamical system being clearly affected by the actual design of the device. This is an important point given our purpose of pre-designing an experimental test rig. That's why a schematic of the experimental setup employed in the above mentioned study is depicted in Figure 3 together with a more classical configuration shown in Figure 4.

Therefore, one can see that the pitch-plunge motion in the left-hand side Figure is realised by rotational motions around two pivot points: the pitching motion is activated by the stepper motor and the associated rotation being along its vertical axis, while the so called heaving motion being in fact a circulatory motion around the vertical axis of the magnetic damper with a radius equal to the length of the horizontal swing rod. On the other hand, the second platform shown in Figure 4 allows for independent pitch and plunging motions, here the purely translational plunging motion being achieved by the motion of the horizontal step motor along the rack via the pinion mounted on it and the rotational motion (pitching motion) is controlled by the second-step motor mounted to the cart [22]. Thus, one can observe that for the system depicted in the left-hand side, the magnetic damper associated to harvesting the heaving energy is not a moving part, thus not affecting the inertia of the heaving motion. On the contrary, since the motion of the heaving has a streamwise component, the uniform flow assumption may not hold depending on the magnitude and the frequency of the plunging and surging flow assumption may be required.

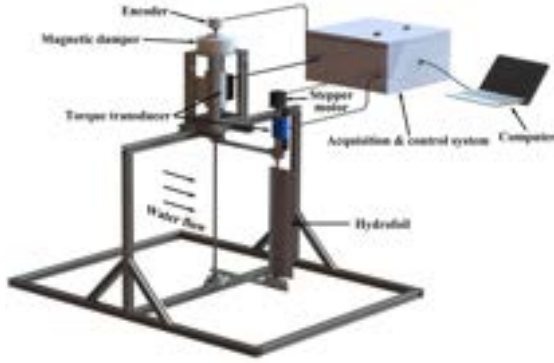


Figure 3: Schematic of the experimental setup under the semi-active mode [17]

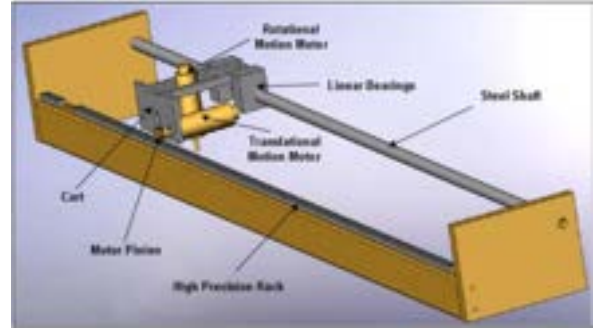


Figure 4: Schematic of the experimental setup of a passively oscillating energy harvester [22]

Passing to the key findings by Zhen Liu in [17], it was firstly demonstrated that the mean power output increases by increasing the activated pitching amplitude up to an amplitude $\theta_0 = 90^\circ$ for some dampers. Additionally, the authors point out that only two reduced frequency were investigated, namely $f^* = 0.06$ and $f^* = 0.10$. Nevertheless, it is interesting to note that by increasing the damping factor for the magnetic damper, there is a region of pitching amplitudes (typically for $\theta_0 = 0^\circ - 40^\circ$ for which the heaving cannot be activated. This is clearly a low point for the magnetic damper since those cases are not associated to energy harvesting, the average net power being negative. By contrary, this is not the case for the electric generator, the heaving motion being triggered no matter the pitching amplitude and the frequency. Despite this low point for the magnetic damper, it was shown that the average power coefficients and the efficiencies for the magnetic damper were higher than the ones related to varying load conditions. Therefore, it was shown that the best performing constant damping yielded a maximum efficiency $\eta = 0.24$ by using $\theta_0 = 80^\circ$ and $f^* = 0.10$.

5.3 Physics and Theory regarding the Operating Regimes

It is known that an airfoil that performs a sinusoidal pitch and plunge motions can either extract power from the flow by using the energy of the free stream, similar to a wind turbine (power extraction regime), or consume energy to propel itself forward (propulsion regime). This depends on the direction of the aerodynamic forces generated by the flow on the airfoil, which could be as a first approximation linked to the effective angle of attack induced by the motion of the airfoil (basing our reasoning on a quasi-steady approach).

In fact, this was shown by a study performed by Jones and Platzer [12] in 1997 in which the energy exchange between a uniform flow and the oscillating airfoil was examined. They found by numerical studies that for energy harvesting to occur, the pitch amplitude must exceed the induced angle of attack due to the plunging motion (or $\alpha(t) > 0$, as depicted by equation 1). Additionally, another study demonstrated that the energy produced can be increased by using 2 foils in tandem so that the foil downstream could benefit of the wake of the one upstream [23].

One peculiar study that examines the potential physics of the two regimes associated to pitching and plunging foils represents the experimental one performed by Gopalkrishnan et al. [24] in 1994. In the paper, the flow around a D-shape cylinder which has sufficiently far downstream (for mitigating the interference with the cylinder associated vortex street formation) a pitching and heaving foil at a frequency close to the Strouhal frequency of the cylinder is analysed.

They suggested that at least 2 modes could be distinguished by varying the relative spacing between the cylinder and the foil so as to change the arrival time of the cylinder vortices at the foil leading edge in order to coincide with different phases in the heaving and pitching motion of the wing. Therefore, the interactions between the upcoming vortices and the vortices generated by the flapping of the airfoil itself can be either constructive in which the vortices are in the same phase and reinforce each other by leading to a stronger reverse Kármán vortex street (thrust type) or destructive, the latter being characteriwed by a phase shift of 180° between the foil-generated vortices and the incoming ones. For the destructive mode, cylinder vortices are repositioned by the foil and they interact with vorticity shed by the foil, which is of opposite rotational sign. Therefore, the resulting vortices have smaller circulation than, or even opposite circulation to the oncoming cylinder vortices, thus drag type Kármán vortex street and

energy extraction by the foil from the cylinder eddies.



Figure 5: Vorticity field for a typical power extraction regime (up) and for propulsion. Mean velocity-profiles are also sketched [13]

It is thus interesting to note that depending on the wake signature, an oscillating airfoil can undergo two operating regimes, respectively power extraction and propulsion. The same phenomenon was also observed by Kinsey and Dumas [13] for an isolated pitching-plunging airfoil in an uniform stream, as depicted by Figure 5.

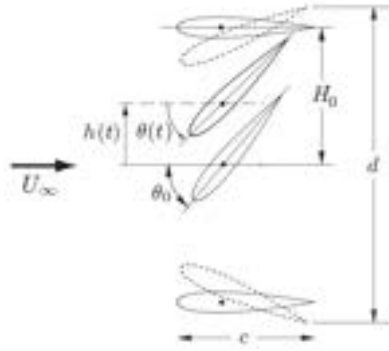


Figure 6: Oscillating airfoil imposed motion [13]

The parameters that describe the motion of the airfoil can be observed in Figure 6. Here, the upstream velocity is denominated U_∞ , the heaving amplitude is h_0 , and the angular position $\theta(t)$, with its associated amplitude θ_0 . Finally, d represents the overall swept displacement of the airfoil, taking into account the projected area of the airfoil in a direction perpendicular to the far free stream velocity. Thus, the motion-induced angle of attack can be expressed as follows:

$$\alpha(t) = \theta(t) - \arctan\left(-\frac{\dot{h}(t)}{U_\infty}\right) \quad (1)$$

where $\arctan\left(-\frac{\dot{h}(t)}{U_\infty}\right)$ represents the induced angle of attack associated with the heaving motion. The effective velocity experienced by the airfoil can be written similarly in eq. (2):

$$V_{\text{eff}}(t) = \sqrt{U_\infty^2 + \dot{h}(t)^2} \quad (2)$$

Since the maximum values obtained over one cycle are expected to have the highest impact on the magnitude of the generated forces, it is worth analyzing both the moment at which they occur, as well as their magnitude. It can be shown that the maximum effective velocity and the maximum absolute effective angle of attack are obtained at approximately quarter period:

$$V_{\text{eff}}(T/4) = \sqrt{U_\infty^2 + (2\pi f H_0)^2} \quad (3)$$

$$\alpha_{\text{max}} \approx \alpha(T/4) = \left| \theta(t) - \arctan\left(-\frac{2\pi f H_0}{U_\infty}\right) \right| \quad (4)$$

The link between the position and the associated angle of attack can be easily observed in Figure 7 (where the apparent movement of the airfoil is from right to left). One can notice that at $t = T/4$ the heaving

movement of the airfoil is directed downwards and the effective angle of attack is negative in the above (green) part of the Figure, thus the vertical component of the resultant aerodynamic force is oriented in the same direction as the movement (the heaving motion is produced by the free stream) (Fig. 7). This regime is a power extraction one and this is the one which will be investigated because a typical device would be fixed in the X direction and harvest energy from the free stream in the Y heaving direction. On the contrary, the airfoil represented in blue exhibits a heaving motion downwards, but the effective angle of attack is positive, thus the vertical component of the resultant is in the opposite direction to the heaving direction. This means that the airfoil is exerting an amount of work on the fluid in order to gain forward-oriented horizontal force (propulsion).

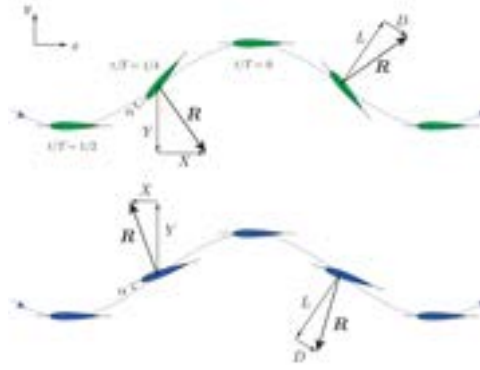


Figure 7: Oscillating airfoil regimes. Green (Power extraction regime $\chi > 1, \alpha(T/4) < 0$)
Blue (Propulsion $\chi < 1, \alpha(T/4) > 0$) [13]

Beyond the physically presented aspects of the two regimes, the nature of the regime (propulsive or power harvesting) can be predicted by the so-called "feathering parameter" [13] defined as the following:

$$\chi = \frac{\theta_0}{\arctan(\frac{2\pi f H_0}{U_\infty})} \quad (5)$$

Practically, $\chi > 1$ may be linked to $\theta_{\max} = \theta(T/4) < 0$, which means extraction regime and $\chi < 1$ for propulsion mode analogically. Finally, $\chi = 1$ is associated with $\theta(T/4) = 0$ which means that the resultant force is a pure drag force (tangent to the apparent trajectory of the airfoil relative to the free stream), thus without any lift component. The authors point here that according to Kinsey and Dumas [13], the above-mentioned condition (the correlation between χ and one particular regime) is a necessary, but not sufficient condition (since this represents a quasi-steady assumption) that places one motion configuration into either propulsion or extraction regime.

6 Power Extraction Efficiency

From an aerodynamic perspective, the efficiency for a Flapping Foil Power Generator is defined as the ratio between the energy generated by the aerodynamic forces and moments on the foil (or airfoil in 2D) over the available energy of the oncoming flow. The power extraction efficiency η is thus presented in equation (6). This definition has been used by Kinsey and Dumas [13], by Quadri and al. [25] and others.

$$\eta_{\text{aero}} = \frac{\overline{P_h} + \overline{P_\theta}}{\frac{1}{2}\rho U_\infty^3 S_w} \quad \text{with} \quad P_h(t) = L(t)\dot{h}(t) \quad \text{and} \quad P_\theta(t) = M_\theta(t)\dot{\theta}(t) \quad (6)$$

Additionally, this can be expressed as well in a non-dimensional form by considering $C_P \equiv \frac{P}{\frac{1}{2}\rho U_\infty^3 S}$, with $S = b \times c$. It can be shown that the equation for efficiency becomes:

$$\eta_{\text{aero}} = (\overline{C_{P_y}} + \overline{C_{P_\theta}}) \frac{c}{d} = \overline{C_P} \frac{c}{d} \quad (7)$$

However, the mechanical aspect of the system is not be taken into account by this equation. Nevertheless, if one wants to focus on the aerodynamics and neglect the mechanical aspects of the system, this form defines the net average power retrieved after one period considering both pitching and plunging motions (the numerator) over the net power of an uniform stream tube that envelopes the swept overall area of the foil (the denominator). $S_w = d \times b$ refers to the swept area, b being the span of the foil. The swept distance is marked here by the parameter d , a more visual meaning being depicted by Figure 6.

Since this paper looks into the aerodynamical performance of a FFPG, but also proposes to perform an optimization for an aeroelastic semi-active system (i.e. mechanical aspects taken into account), it is worth defining the efficiency formula that will be considered in this case. Given the conducted literature review in section 5, the semi-active FFPG is a system that imposes a pitching motion, therefore consumes energy for pitching and harvests energy from the resulting plunging motion. Additionally, the effective energy harvesting device related to the plunging motion is modeled in this work by a viscous damper. Therefore, the formula for the efficiency is:

$$\eta = \frac{P_h + P_\theta}{\frac{1}{2}\rho U_\infty^3 S_w} \quad \text{where} \quad P_h = C_h \dot{h}^2 \quad (8)$$

The authors point here that for the following approach regarding the semi-active system, all the power that is linked to the pitching motion is considered consumed and the power linked to heaving is seen as produced (which makes sense for heaving since it results from the motion). This approach is taken following a practical reasoning for the pitching motion, since even though in theory there may exist a region where the power associated to the pitching is positive, the real system is assumed to still consume energy: the controller acting no more like a generator, but like a brake.

7 Aerodynamics of a Flapping Airfoil Power Generator

7.1 Pitch and Plunge Airfoil

The aerodynamical system considered is a two-degrees of freedom pitch and plunge airfoil. The system is able to translate on the \vec{z} axis and to rotate around the \vec{y} axis. A steady flow associated to a freestream velocity U_∞ is oriented according to the \vec{x} axis. This two dimensional system will then be scaled to a tridimensional foil with a fixed span b . The tridimensional aerodynamics effects will be neglected by the current approach. A sketch of the two-degrees of freedom pitch and plunge airfoil is provided in Figure 8.



Figure 8: Sketch of the two-degrees of freedom pitch and plunge airfoil.

θ is the angle between the airfoil and the frame of reference and h corresponds to the displacement on the \vec{z} axis. The airfoil selected is a *NACA0012*.

Optimizing a Flapping Foil Power Generator may involve many variables and some need to be fixed for the current study. The freestream velocity and the chord have been both fixed to a specific value. In fact, they are assumed to not drive the current investigation. Nevertheless, these two parameters are defining the Reynolds number and the appearance or not of compressibility effects. In order to be able to use the numerical tools mentioned in the following, the only constraint directly imposed is to only deal with incompressible flows which is easily satisfied in the scope of the current study.

A freestream of $U_\infty = 10 \text{ m.s}^{-1}$ and a chord of $c = 0.25 \text{ m}$ have been selected. The choice of velocity was driven by looking at the range of velocities compatible with a possible utilization of such a system. The fluid is assumed to be the air, $\rho = 1.225 \text{ kg.m}^{-3}$, in the current approach but this could be easily modified. Such Flapping Foil Power Generator are often designed to operate in water due to its high density and the possible improvements that high density flows can bring in term of energy extraction and frequency for the motion.

These values of the freestream velocity, density and chord, lead to a Reynolds number of approximately $\text{Re} = 1.7 \times 10^5$. The Reynolds number is a quantity important to assess because its is defining the different tools that could be used or not for the current investigation. From the literature, it is possible to see that this range of Reynolds number is not really covered for such FFPG. The reason is that it is very challenging, even sometimes impossible in term of computational resources to conduct some studies at these Reynolds numbers with numerical method like LES (Large Eddy Simulation) or like DNS (Direct Numerical Simulation), often assumed more accurate than low order models.

The current study will address this range of Reynolds number by using low-order method to predict the aerodynamical forces and all the quantities related to such FFPG systems. Since the accuracy of such method is not always guarantied due to their inherent assumptions and limitations, a validation step will have to be carefully performed to assess the validity of the results provided.

7.2 LESP Discrete Vortex Method (LDVM)

7.2.1 Theory

7.2.1.1 Discrete Vortex Method (DVM) The Discrete Vortex Method (DVM) originally solves an inviscid vorticity and stream function form of the Navier-Stokes equations [26]. In the field of theoretical and computational fluid dynamics, this form of the Navier-Stokes equations is often used. As mentioned by [27], in principle, an inviscid incompressible flow can be specified entirely by the combination of a potential flow and the kinetics generated by the local rotation of the fluid. The reason of considering this formulation is that under some assumptions like, two-dimensional inviscid and incompressible Newtonian fluid of constant density, the vorticity transport form may simplify the solving of the equations. These simplifications could not be made if the Navier-Stokes equations are expressed with the velocity and the pressure.

Among the approaches using the vorticity transport form, two approaches can be used: the Eulerian approach and the Lagrangian approach. In Lagrangian approach, the observer follows an individual fluid particle as it moves through space and time. In the Eulerian approach, the observer focuses on specific locations in the space through which the fluid flows as time passes. The Discrete Vortex Method is derived upon the Lagrangian approach [28].

The flow field is discretized into a series of vortex that are tracked in the flow. The Discrete Vortex Method is thus a grid-free approach which allows to investigate a wide range of problems, including those with stationary and moving bodies [28]. Potential theory methods can be used to impose solid boundaries satisfying an inviscid no-penetration condition. Panel method or a conformal transformation are commonly used for this purpose, both of them having advantages and disadvantages [27].

The vortexes are shed from the trailing edge, and their strengths are calculated iteratively such that the flow is tangential to the airfoil surface and such that Kelvin's circulation theorem is satisfied [29]. This way of modeling of the flow allows to obtain the aerodynamical forces applied on the geometry considered under some assumptions.

The effects of viscosity can be taken into account by making some modifications to the inviscid model [27]. The viscous no-slip boundary condition (i.e. the physical effect that induces vorticity creation at the boundaries) can be modeled by introducing in the flow new vortexes of the correct strength. Moreover, a diffusive component needs to be included to model the additional Laplacian term in the Navier-Stokes equations.

7.2.1.2 Separated Flows and Dynamic Stall Applicability From the literature review, one can understand that the optimal Flapping Foil Power Generator are currently the ones undergoing significant amplitudes, mainly for the pitch. This leads to high angles of attack and thus to significant flow separation on the foil. If one want to optimize such system, a numerical approach able to model the physics of such flows is required.

Due to the assumptions made in the derivation of classical Discrete Vortex Methods or others theory trying to model unsteady airfoils, they are mainly limited to small amplitudes and attached leading-edge flows.

However, Discrete-vortex methods have been used extensively to model unsteady separated flows through various improvements and modifications. In the scope of this study, the choice has been made to use the Discrete Vortex Method with a novel shedding criterion modeling massively separated and vortex-dominated flows, proposed by Ramesh et al. [29]. They proposed a leading-edge suction parameter (LESP) to determine the onset, growth, and termination of Leading Edge Vortices (LEV). This parameter allows to model flows that are characterized by LEVs shedding and thus regimes such as dynamic stall.

One may notice that the primary limitation of LDVM (LESP Discrete Vortex Method) is the choice for the value for the critical LESP. It is a single parameter supposed to represent simultaneously the shedding of the LEVs and the Reynolds number of the flow while being linked to the shape of the airfoil. Ramesh et al. [29] carefully mentioned in their publications that this critical LESP should be set based on experimental or numerical results for the flow and airfoil considered. For the current study, such procedure was not performed, and the critical LESP value was fixed to $LESP_{crit} = 0.14$ due to the airfoil selected (*NACA0012*) and the Reynolds number investigated ($Re = 1.7 \times 10^5$). $LESP_{crit} = 0.14$ was found according to the values mentioned by Ramesh et al. [29] for some airfoils and Reynolds numbers. The value corresponding the most to the current system has been selected. The authors are aware of the significant source of uncertainty regarding the value choose for the critical LESP. This might indeed lead to inaccurate flow predictions if the critical LESP does not correspond to the case studied. Further discussions will be conducted during the validation of LDVM in 7.2.3.

7.2.2 Implementation

Ramesh et al. [29] published LDVM as an open-source code. It is essentially a Fortran script which is taking two input files, one for the kinematics and one for the solver settings. An output file containing the aerodynamic forces acting on the airfoil is provided.

For the current study, Python has been selected mainly reasons like its simplicity and all the library publicly available which will be used in the following (PyTorch, Pymoo, etc.). Moreover, Python is open-source, which is a real advantage.

However, one can understand that LDVM is not developed to be compatible with Python and one cannot afford to run every case that are going to be investigated in this study manually and then to import every results in Python. On the other hand, the authors assumed that Fortran is not the best choice for what will be done further in the study (neural networks, optimizations). In fact, most of the library considered in this work are not compatible with Fortran.

In order to tackle this problem, LDVM has been encapsulated in Python, meaning that Python is running the Fortran script containing LDVM. Every time that a motion needs to be solved with LDVM, Python creates a temporary folder where the source code is copied and executed. The results are then loaded and available as an object in Python. This way of tackling the problem is not the most efficient but otherwise LDVM (i.e. the original script) would need to be translated in Python. The authors made the choice to keep the LDVM script as it was published by Ramesh et al. [29]. The computational overhead comes from the creation of a temporary folder, from the writing of the kinematic and setting files and from the loading of the results. However, all of these actions are assumed to require a computational time significantly lower than the time needed by the Fortran script to solve the motion.

7.2.3 Validation

Despite the fact that the ability of LDVM to capture the aerodynamic features associated to leading edge vortexes was rigorously validated by the authors [29] for various airfoil shapes, Reynolds numbers and motion types, their validation does not exhaustively cover the entire range of possible cases. The authors remind here that the essential parameter for each case is represented by the critical LESP (value beyond which the formation of LEV occurs) which is dependent on the airfoil type and the Reynolds number. The critical LESP is nevertheless invariant to the kinematics. This means that once outside the verified validity range regarding either the airfoil type or the Reynolds number, one cannot claim that the code is producing accurate predictions for the investigated case.

Two ways of solving this problem were proposed by the authors. The first one consists in establishing empirically its value by considering more refined numerical simulations. The second way consists in finding the value that matches the best the physics or by using the data available from the literature. The second approach was selected. The critical LESP was chosen from the existing database created by Ramesh et al. [29].

For the validation of LDVM (for the purposes of this study), three cases are considered for comparing the associated predictions: a pure pitching case performed experimentally by Ôtomo et al.[30], a pitching and plunging case conducted by Kinsey et al. [13] on which a sensitivity study on LESP is performed and lastly a global comparison between a sinusoidal and a non-sinusoidal pitching motions from Xiao et al. [15].

7.2.3.1 Pure Pitching In the study performed by Ôtomo et al.[30], unsteady time-resolved force and velocity field measurements are performed on a purely pitching hydrofoil in a water channel facility.

For their experiments, a NACA0018 airfoil is used, the corresponding Reynolds number given the incoming flow velocity and the chord size is $Re = 3.2 \cdot 10^4$. Additionally, the pitching axis is located at quarter-chord from the leading edge. The reduced frequency is $k = 0.22$. The critical LESP value considered for this comparison is 0.18, this value is corresponding to the closest validated case by its authors for a SD7003 airfoil under a $Re = 3 \cdot 10^4$.

Comparisons between the phase averaged lift coefficients extracted from the data provided by [30] and the lift coefficient predicted by LDVM are provided in Figure 9. An additional set of data for the C_L and C_M respectively is provided by considering a very high value for the LESP parameter. This value theoretically corresponds to a case in which no leading edge vortex is shed and it is shown to emphasize the significant change in the predictions due to this phenomenon.

By looking at the symmetrical motion for $\theta_0 = 32^\circ$, one can see that the lift coefficient is pretty close to the one found experimentally for both LESP values, except for a significant overshoot around the maximum pitching angle reached and equivalently a slight underestimation close to the minimum pitching angle (pitching down phase). Additionally, the same behavior could be observed for the asymmetrical case even if the maximum lift coefficient is better captured. When it comes to the pitching moment, large discrepancies could be observed between the two LESP values for all the cases considered. Unfortunately, experimental data is unavailable regarding the pitching moment.

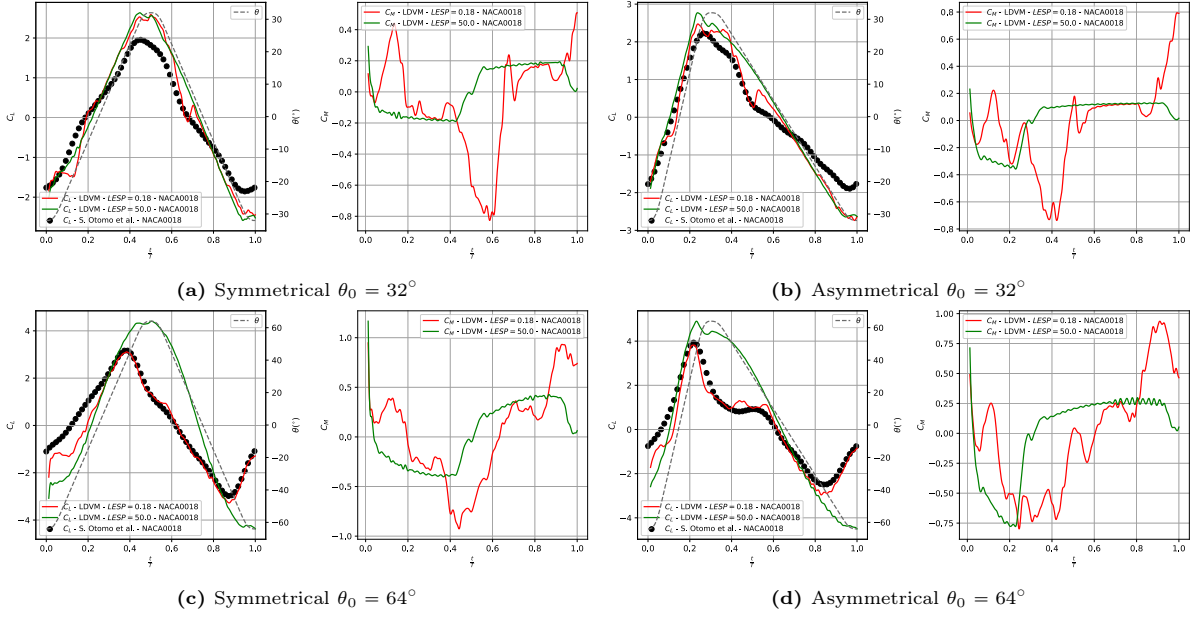


Figure 9: Lift Coefficient C_L and Moment Coefficient C_M for multiple pitching motions. The pitching motions are depicted in grey.

Regarding the highest amplitude case depicted in Figures 9c, 9d, one first important note is that remarkable differences appear in the lift coefficients between the predictions with the two LESP values. This may indicate the presence of more leading edge vortexes shed for the highest amplitude case that does not appear for the $\theta_0 = 32^\circ$ case. Moreover, the simulation with critical LESP = 0.18 has a satisfactory match with the experimental data, it displaying an underestimation during the pitch-up motion for the symmetrical case that slightly appears as well for the asymmetrical one. Additionally, for the asymmetrical case, two minor bumps in lift appear compared to the experimental value between a fraction of time equal to 0.4 to 0.5 of the period.

7.2.3.2 Sensitivity Analysis on the LESP Parameter In this paragraph, a comparison for a pitching and plunging case is provided between LDVM and the data from Kinsey and Dumas [13], the analyzed motion being the best performing case found in their study, namely the case in which $\theta_0 = 76.3^\circ$ and $f^* = 0.14$. For this comparison, the pitching axis is located at one third of the chord according to their study. The authors remind here that their study is performed at a quite low $Re = 1100$ and for a NACA0015 airfoil. Therefore, the best matching critical LESP value was considered to be $LESP = 0.21$ for a NACA0012 airfoil and the same Reynolds number.

More LESP values around the baseline value were used in order to assess the sensitivity of this value on the resulted forces, as depicted in Figure 10. Interestingly, one could qualitatively see that lower values of critical LESP (particularly $LESP = 0.075$ displayed by the orange line) compared to the baseline match the vertical force coefficient slightly better, especially around $t/T = 0.1$ and $t/T = 0.6$. However, when it comes to the prediction of the moment coefficient, the baseline captures better the trend (especially around $t/T = 0.6$) despite its differences in magnitude as compared to the data from Kinsey and Dumas.

Lastly, a mapping of the efficiency in the parametric space (f^*, θ_0) is performed according to the one provided by Kinsey and Dumas [13] and it is shown in figure 11. One striking point can be observed by looking at this graph, and that is the maximum efficiency achieved η_{aero} that peaks at about $\eta_{aero} = 80\%$, a value much higher than the maximal one obtained by Kinsey, which is $\eta_{aero} = 36.4\%$. We highlight here that the highest efficiencies are achieved for fairly high pitching amplitudes $\theta_0 \approx 75^\circ - 85^\circ$ and for an operating condition of approximately $k = 0.53$, these cases involving high angles of attack. This unsatisfactory high predicted efficiency can be due to the limitations of LDVM itself such as the formation of thick or separated boundary layers that are not modeled by the theory.

All in all, for this airfoil and around this Reynolds number, the trend of the predictions is more or less conserved for all investigated LESP values, the baseline fitting quite well the CFD results. Nevertheless, given the good prediction of the trend, but not always the accurate prediction of some global parameters (e.g., η_{aero}), one should note that a comparative optimization could be performed, the global performance

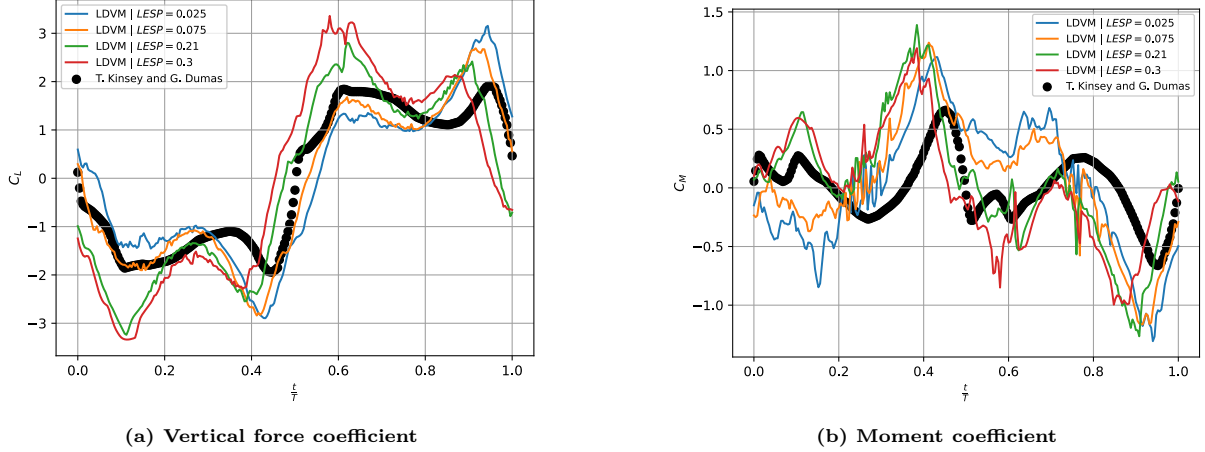


Figure 10: Comparison of C_l and C_m over one period between LDVM and data from Kinsey & Dumas [13]

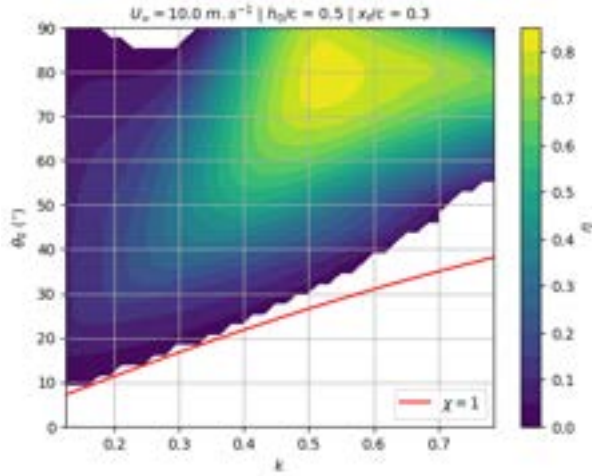


Figure 11: Parametric Analysis conducted on the Aerodynamic Efficiency η_{aero} as a function of the reduced frequency k and the pitching amplitude θ_0 . The results are obtained with LDVM.

of that case having chances of being biased by comparison to the actual performance.

In fact, is it not even expected to retrieve a perfect match compared to viscous CFD simulations or with experimental data since the LESP has been created in order to capture the phenomenon marked by its name, LDVM being essentially an inviscid solver that is tuned to capture the leading edge separation behavior which has a significant impact on the predictions. Nevertheless, the friction drag is also not predicted, this being a potential source of error.

7.2.3.3 Non Purely Sinusoidal Motions A last validation analysis is performed by comparison with results obtained by Xiao et al. [15] with a compressible unsteady solver. In their study, a sinusoidal heaving motion coupled with a trapezoidal-like pitching motion around an axis lying at $x_c = c/3$ are analyzed for power extraction. A NACA0012 was used at a Reynolds of $Re = 10^4$ and the critical LESP was chosen again to match as much as possible these conditions.

As stressed in subsection 5.3, it was shown that the energy extraction capabilities are lined to the magnitude of the effective angle of attack α_{eff} . Nevertheless, since this value varies in time, a more simple value which is time invariant was chosen in this study for assessing the potential of power extraction. Instead, the nominal angle of attack α_0 as depicted in equation 9:

$$\alpha_0 = \theta_0 - \arctan\left(\frac{\omega h_0}{U_\infty}\right) \quad (9)$$

A parametric study was then performed by changing mainly three parameters: β for observing the impact of the trajectory (further explanations about the link between β and the associated motion are given in section 5.1 or in the authors paper [15]), α_0 to assess the impact of the pitching amplitude and St , the

Strouhal number representing the impact of the frequency. The typical effect of β on the trajectory and on the effective angle of attack α_{eff} are displayed in Figures 12 and 13 respectively.

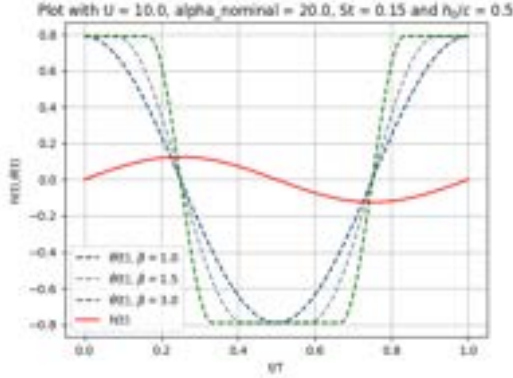


Figure 12: Typical variation of instantaneous $\theta(t)$ and $h(t)$ profile in one period for different β using the function from Xiao [15]

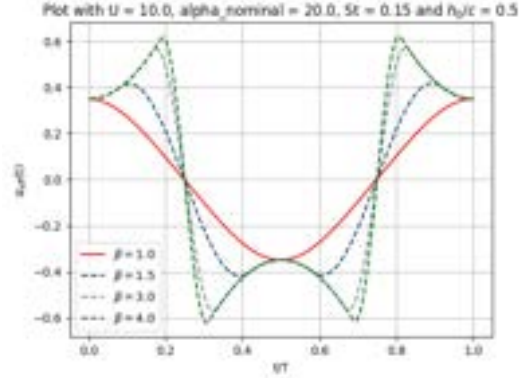


Figure 13: Typical variation of instantaneous effective angle of attack $\alpha_{\text{eff}}(t)$ profile in one period for different β using the function from Xiao [15]

By contrast to the previous validations when a local time-dependent comparison of C_L and C_M was accomplished, a global comparison of the net mean power extraction coefficient C_P between LDVM and the study mentioned previously is conducted. As it is shown in Figures 14 and 15, an exhaustive comparison is performed with the results from Xiao [15] by computing C_P for multiple Strouhal numbers varying from 0.05 to 0.25 with a step of $\Delta St = 0.05$, a linear interpolation being done between the associated C_P values as shown by the continuous lines. This analysis was performed for two nominal angles of attack, $\alpha_0 = 10^\circ$ (Fig. 14) and $\alpha_0 = 20^\circ$ (Fig. 15). To sinusoidal (depicted by the black lines $\beta = 1$) and non purely-sinusoidal (depicted by the red lines $\beta = 1.5$) pitch and plunge motions were also included.

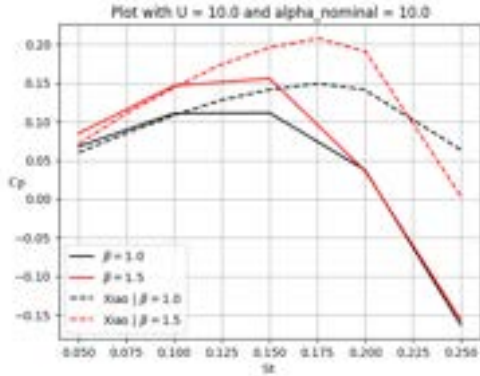


Figure 14: Variation of the net coefficient of the mean power extracted C_P over one period for various β versus St with $\alpha_0 = 10^\circ$. LDVM (continuous lines) and Xiao [15] (dashed lines).

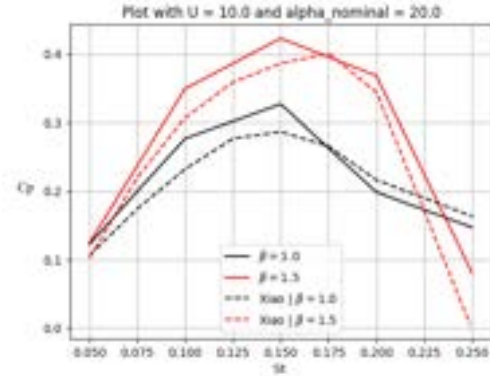


Figure 15: Variation of the net coefficient of the mean power extracted C_P over one period vs St with $\alpha_0 = 20^\circ$. LDVM (continuous lines) and Xiao [15] (dashed lines)

Looking at the case where $\alpha_0 = 10^\circ$, one can see that the C_P values match perfectly with the reference between $St = 0.05$ and $St = 0.1$ but then both $\beta = 1$ and $\beta = 1.5$ cases (continuous black and red lines) are diverging from the dashed reference lines. Nevertheless, the trends are similar, LDVM showing a peak in C_P for both analyzed β values at $St = 0.15$, while the reference cases peak at roughly $St = 0.175$, the difference between the two St value being potentially due to the larger discretization step ΔSt . Regarding the highest α_0 case presented in Figure 15, one could observe a way better match with a very low discrepancy in C_P between both purely sinusoidal and non-sinusoidal cases. Additionally, the C_P peaks are quite perfectly captured with a perfect match in St number for the non-sinusoidal case (black lines) and with the same offset of $\Delta St = 0.025$.

To conclude, the LESP-modulated Discrete Vortex Method has proven to be a fast and surprisingly accurate model if the correct LESP value is used. Therefore, one should wisely make the choice of the critical LESP corresponding to both an airfoil and an operating Reynolds number.

7.3 Unsteady Aerodynamic Model using Deep Learning

The LESP Discrete Vortex method proposed by *Ramesh et al.* [29] has been validated as the method that will be used in this study to evaluate the aerodynamical forces acting on the airfoil. The advantages and limitations of this method are known and will be kept in mind for the following study, especially for the amplitude of these forces that will be taken only as an approximation of the reality.

The principle objective is now to develop an aeroelastic model which could be used later to optimize a Flapping Foil Power Generator. In order to achieve this, a coupling between an aerodynamical and a structural model is required. However, as already mentioned, the LDVM is a Fortran script which takes input files for the settings and the kinematics and provides output files containing the aerodynamical forces acting on the airfoil. To be able to couple it with a structural model, the aerodynamic forces and the motions would need to be computed simultaneously at numerous time steps throughout a period. Additionally, the kinematics and the aerodynamical forces are fully coupled, meaning that one can influence the other. At this stage, one can understand that coupling LDVM with a structural model is impossible in its current form (Fortran script) because the kinematics and the aerodynamic forces cannot be computed simultaneously. The only way to achieve a coupling would be to modify the original script, which is not done in this study. The authors made the choice to keep the LDVM script as it was published by Ramesh et al. [29].

To tackle this problem, one could think about building a neural network trained on LDVM outputs. In this case, the inputs would be the kinematics and the outputs, the aerodynamic forces. Neural networks represent one of the available tools to perform this task. They are known to be efficient at predicting accurately the outputs corresponding to some inputs. The only limitation is that its prediction is valid only if the inputs are included in the bounds of values used for the training. Corban et al. [31] used neural networks for a similar problem. They show that using CFD to generate a dataset and then optimizing the kinematics for a flapping wing with the use of a neural network trained on this dataset was very efficient.

7.3.1 Multilayer Perceptron Architecture (MLP) and Inputs

The neural network is a feed-forward neural network (FNN), coded and trained using Pytorch (Paszke et al. 2019 [32]). The FNN employed here is a MLP, composed of successive layers of neurons. The output layer size is 2, meaning that the neural network will predict two outputs at an instant t : the lift and the pitching moment acting on the airfoil.

To make a prediction for an output at a time t , the neural network is taking as input a vector \vec{X} , which is composed of the state vector \vec{x} and additional parameters in this case. Its expression is shown in equation (10). The same approach as Corban et al. [31] was implemented, where m represents the number of previous states which will be used for the prediction and τ refers to the number of time step of the current predictions and the previous states considered. Corban et al. showed the relevance of this approach with an optimization of a flapping wing kinematics which is not that far from the topic addressed by this study. Such a method has also been shown sufficient to replicate results from high-order numerical codes, as for instance by Alguacil et al. (2022) [33] for acoustic waves propagation.

The state vector \vec{x} is composed of the pitching angle θ , the angular velocity $\dot{\theta}$, the heaving position h and the heaving velocity \dot{h} as shown in equation (11). The reduced frequency k and the position of the rotational axis x_f are also given as inputs for the neural networks. The output vector \vec{Y} , contains the lift coefficient C_L and the pitching moment coefficient C_M acting on the airfoil at the instant t , as shown in equation (12). Corban et al. [31] mentioned that adding additional derivatives of the pitch angle could improve the prediction performance. However, the state vector $\vec{x}(t)$ only contains the first derivatives since it has been shown sufficient in the current study.

$$\vec{X}(t) = [k, x_f, \vec{x}(t), \vec{x}(t - \tau dt), \dots, \vec{x}(t - (m - 1)dt)] \quad (10)$$

$$\vec{x}(t) = [h(t), \dot{h}(t), \theta(t), \dot{\theta}(t)] \quad (11)$$

$$\vec{Y}(t) = [C_L(t), C_M(t)] \quad (12)$$

Here, m and τ should be determined by performing a partial grid search as mentioned by Corban et al. Increasing m causes an increase in neural network size, as the input is larger, more neurons are needed to process it. This affects the training duration and prediction time once trained, thus m should be chosen as low as possible. There is also an optimum value for τ which would allow increase the accuracy of the prediction by the MLP. Such analysis was not conducted in the scope of this study. However the topic investigated by Corban et al. appears to be very similar to the current Flapping Foil Power Generator. The same values for m and τ have been used: $m = 3$ and $\tau = 9$.

The architecture of the neural network is the following: three hidden layers, with respectively 512, 1024 and 512 neurons, which correspond to a total of approximately 1 million tunable parameters. Each neuron activation function is a ReLU.

7.3.2 Training and Validation

A dataset containing multiple reduced frequency k , multiple rotational axis locations x_f and multiple pitching amplitude θ_0 has been generated. Two of these parameters (k and x_f) are directly inputs of the neural networks and θ_0 is contained in the state of the system $\vec{x} = [h(t), \dot{h}(t), \theta(t), \dot{\theta}(t)]$. In order to reduce the dimension of the problem, the heaving amplitude h_0 and the freestream velocity U_∞ were fixed to $h_0/c = 0.5$ and $U_\infty = 10.0 \text{ m.s}^{-1}$. The motions are sinusoidal with a phase shift of $\pi/2$ between the pitch and the plunge, as it yields the best efficiency as mentioned by Kinsey and Dumas [13]. The kinematics used to generate the datasets are shown in equations 13 and 14.

$$h = h_0 \cos(\omega t) \quad (13)$$

$$\theta = \theta_0 \sin(\omega t) \quad (14)$$

Table 1 provides the range of values covered for the three main parameters driving the dataset generation. A tridimensional equally spaced grid has been set up and defines all the motions covered. For every motion, meaning for every combination of $\{k, x_f, \theta_0\}$, a different kinematic results and is run with the LDVM Fortran script encapsulated in Python. The forces predicted by LDVM are then used to build a dataset corresponding to the inputs and outputs of the neural network (\vec{X} , m , τ , etc.). For each motion, the kinematic is discretized in 1000 time steps. From Table 1, it is possible to see that $30^2 \times 14 \times 1000 = 12.6$ millions pairs of inputs/outputs that have been generated for building the dataset.

| Parameters | Values | Steps |
|------------|------------------------|-------|
| k | 0.039 – 0.785 | 30 |
| x_f/c | 0.05 – 0.95 | 14 |
| θ_0 | 0.0° – 90.0° | 30 |
| U_∞ | 10.0 m.s ⁻¹ | - |
| h_0/c | 0.5 | - |

Table 1: Ranges considered for the generation of the dataset.

It worth to be noted that running LDVM for one motion required a duration of the order of magnitude of 20 seconds. One can clearly see that if the dataset is generated sequentially, the computational time is around 3 days. The use of parallel computing and supercomputers allowed to reduce this time. Tasks that are independent from each other are relatively easy to parallelize. In fact, full parallelization can be achieved since all the motions considered here are independent. The MPI (Message Passing Interface) library [34] has been used. With 4 nodes (*CPU Intel Xeon E5-2670v3, 24 cores, 64 Go RAM*), the time to obtain a dataset is reduced to approximately 1 hour and 10 minutes.

Another important note is that LDVM is a numerical tool subjected to many numerical instabilities. If one tries to compute one period, $0 < t/T < 1.0$, and then to compute two periods, $0 < t/T < 2.0$, of the same motion, the outputs provided with LDVM will not be the same. However, the authors assumed that for $t/T > 1.0$, the LDVM outputs are not changing anymore (i.e. transient state finished). For the following use of LDVM (dataset generation included), all the motions have been computed for two successive periods and only the results corresponding to the second period have been considered. Another consequence of these numerical instabilities is that for some motions the outputs of LDVM include some local overshoots and other noisy contents. This has to be linked with the Vortex Discrete Method and the removal of the initial vortex in the wake. Because the circulation, and thus the aerodynamical forces

depends on this initial vortex, when it is removed from the simulation, this lead to large overshoots in the forces. To tackle this problem, the outputs of LDVM are filtered with a low-pass filter because these instabilities are assumed to be mainly at high frequency (i.e. frequency significantly higher than the frequency of the motion). This allow the obtain clear and usable outputs from LDVM for the dataset generation for instance. One must know that this issue only concerns LDVM (i.e. not the neural network).

This dataset of motions (containing 12600 motions) was split in three parts. 84% of the motions are used to train the neural network by updating the weights and biases in each neuron. 8% are used for the validation to check the neural network performance during the training on a set of data on which the weights are not updated. This is useful to prevent the overfitting (i.e. the memorization rather than learning) of the training data. The last 8% are used to test the final network on unseen data and compare the trained models.

The neural network has been trained for 40 epochs, with a batch size of 3840. The optimizer used to train the weights is Adam, with a learning rate of 10^{-4} . The loss is the mean square error (MSE). The implementation of the optimizer and loss function has been taken from PyTorch [32]. The training has been performed with one graphic card *Nvidia A100-PCIE-40Gb* (CUDA 12.4) and lasts approximately around 3 hours.

7.3.3 Performance Metric

In order to test the neural network, a mean \bar{R}^2 score over the motion dataset dedicated for testing has been computed. The implementation of the R2 score by Scikit-Learn has been used [35]. The test of the neural network led to a mean $\bar{R}^2 = 0.979$, which is assumed to be sufficient for the current study. One must keep in mind that this value represents the accuracy of the neural network compared to its reference data, and could be increased by conducting further investigation on the architecture of the neural networks and its inputs.

For a visual illustration of what the neural network is able to do, three different motions (randomly selected and not included in any datasets) have been predicted with the neural network and compared to the LDVM predictions which are acting here as reference. The purpose of the neural network is indeed to reproduce accurately the predictions of LDVM with some generalization capabilities to further be incorporated in an aeroelastic model. One can see that the neural network is well predicting the lift coefficient C_L and the pitching moment coefficient C_M according to LDVM outputs. However, this is only a local qualitative test based on visual verification, only the mean \bar{R}^2 score mentioned previously proving the effectiveness and accuracy of the neural network.

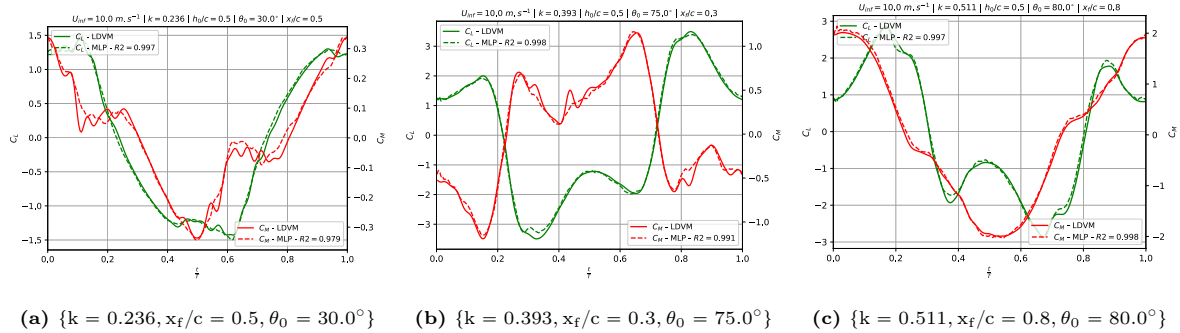


Figure 16: Lift Coefficient C_L and Moment Coefficient C_M predicted by the neural network. Comparison with the outputs from LDVM for the corresponding kinematics. R2 scores are provided for every motions and every quantities.

To conclude this section, the neural network is now trained and able to reproduce accurately the prediction of LDVM which has been validated according to experimental and numerical data. However, as already mentioned in 7.2.3, the authors are aware of the limitations related to LDVM predictions, especially regarding the magnitudes of the forces. This neural network will be later used to develop an aeroelastic model of a Flapping Foil Power Generator.

7.4 Parametric Analysis and Single-Objective Optimization

Before diving in the development of the aeroelastic model, it would be interesting to find the optimal motion under an aerodynamical point of view. This will allow to reduce the number of variables for the

final optimization of the full aeroelastic system. The idea would be to fix the value of the location for the rotational axis x_f and the pitching amplitude θ_0 corresponding to the optimal motion found for the aerodynamical system. The freestream velocity will be kept constant, at $U_\infty = 10.0 \text{ m.s}^{-1}$ as well as the heaving amplitude $h_0/c = 0.5$. The reduced frequency will be investigated in this section but let as a variable because its optimal value is strongly linked with the structural parameters (damping, stiffness, etc.) as it will be shown later.

7.4.1 Parametric Analysis

The performance of the investigated motions will be judged based on their aerodynamic efficiency η_{aero} . The way of defining this efficiency has been mentioned in section 6. One should know that the aerodynamic efficiency η_{aero} is not defined in the same way as the efficiency η for a semi-active Flapping Foil Power Generator.

A parametric analysis on the aerodynamic efficiency η_{aero} was conducted for multiple reduced frequencies k , multiple pitching amplitudes θ_0 and multiple locations for the rotational axis x_f/c . Results are shown in Figure 17. One can notice that the values of the efficiencies are extremely high. As mentioned previously, this is one of the limitations of LDVM, the amplitudes of the forces are over-predicted for some kinematics. However, these limitations are known and it can be assumed that the trends of the values are well captured as shown by the previous validation.

One could observe from Figure 17 that the highest efficiencies (i.e. optimal motions) are obtained for $0.2 < x_f/c < 0.4$ and for $70.0^\circ < \theta_0 < 85.0^\circ$ (Figs. 17b, 17c, 17d). The reduced frequency also plays a huge role in the efficiency of the corresponding motions. The range $0.5 < k < 0.65$ leads to the highest efficiencies.

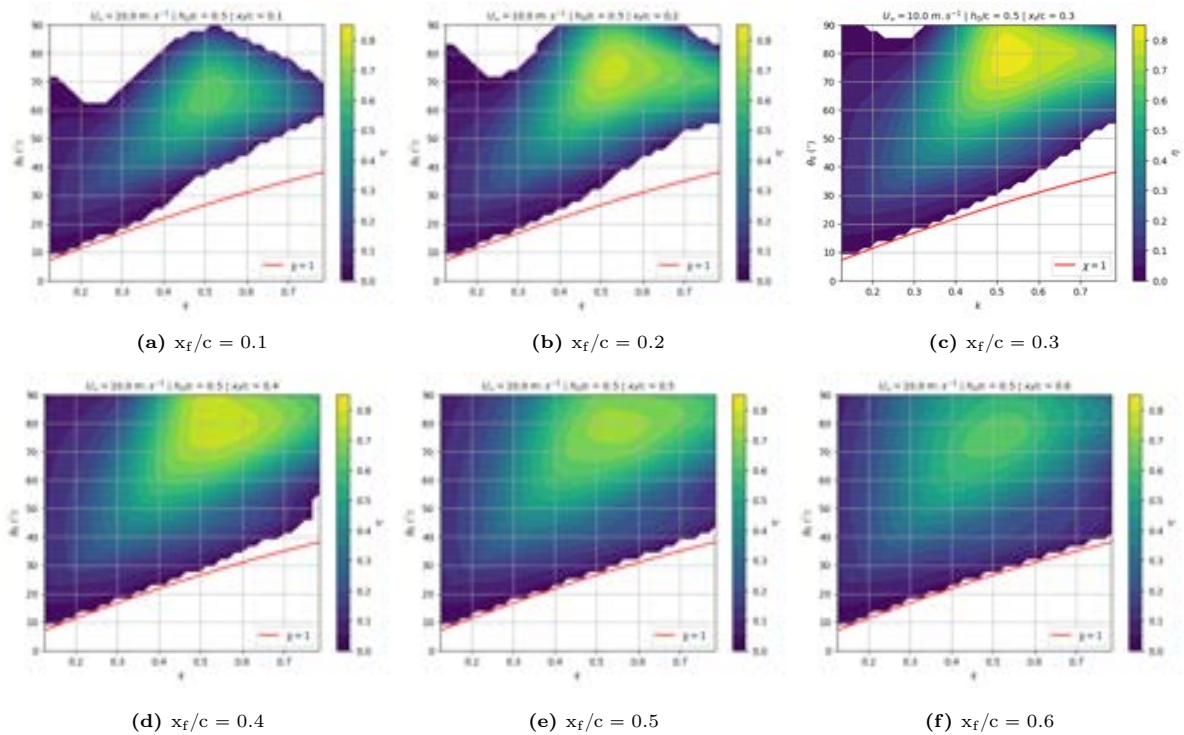


Figure 17: Parametric study conducted on the aerodynamic efficiency η_{aero} . Multiple values of reduced frequencies k , of pitching amplitudes θ_0 and of locations for the rotational axis x_f/c are investigated. Efficiencies for which $\eta_{\text{aero}} < 0$ have been excluded.

In Figure 17, the feathering parameter χ was introduced. The feathering parameter is supposed to indicate the limit between the propulsion and energy extraction mode associated to such Flapping Airfoil Power Generator system under quasi-steady assumptions. More information about the feathering parameter can be found in Kinsey and Dumas [13] paper on a similar subject. This parameter is here shown as an indication that the results follow the trend of the quasi-steady assumptions with some deviations. These deviations are however expected because LDVM does not obey the quasi-steady assumptions.

7.4.2 Problem Formulation

In order to define this optimal motion, a single objective optimization has been conducted based on the aerodynamical efficiency η_{aero} . The optimization problem has been formulated in equation (16). The search space of the current problem is defined in (15).

$$\begin{cases} S = [0.039, 0.785] \times [0.05, 0.95] \times [0.0^\circ, 90.0^\circ] \\ x = \{k, x_f/c, \theta_0\} \text{ with } x \in S \end{cases} \quad (15)$$

$$\begin{cases} \underset{x \in S}{\text{minimize}} & -\eta(x) \\ \text{s.t.} & |P_c| - |P_e| < 0 \end{cases} \quad (16)$$

7.4.3 Optimization using Genetic Algorithm

The neural network is coupled with a genetic algorithm used to perform a single-objective optimization of the motion. The standard genetic algorithm (GA) is used from the Pymoo library [36]. Genetic algorithms are based on the survival of the fittest principle: like in natural evolution, the fittest individuals live through the generations. The stochastic nature of the genetic algorithm makes them suitable in evading local optima, which are typically encountered in such non-convex optimization problems.

Each individual is composed of the three parameters $[k, x_f, \theta_0]$. The bounds of the search space are defined in equation (15). The population is composed of 100 individuals and 50 offspring are generated for each generation. The cross-over method is the simulated binary cross-over, and the mutation method is the polynomial mutation (further details can be obtained from [36]).

The best motion is provided in Table 2. The freestream velocity was kept fixed at $U_\infty = 10.0 \text{ m.s}^{-1}$ as well as the heaving amplitude at $h_0/c = 0.5$.

| Parameters | Values |
|------------|--------------|
| k | 0.531 |
| θ_0 | 79.5° |
| x_f/c | 0.32 |

Table 2: Optimal Kinematic and Parameters found by the Genetic Algorithm based on the Aerodynamic Efficiency η_{aero} . $U_\infty = 10.0 \text{ m.s}^{-1}$. $h_0/c = 0.5$.

The results showed in Table 2 are coherent with the observations made in the parametric analysis as in Figure 17.

In order to conclude this section, the important information that one should keep in mind is that the optimal Flapping Airfoil Power Generator is obtained for $x_f/c = 0.32$ and $\theta_0 = 79.5^\circ$ given the other quantities already fixed. The pitching amplitude and the rotational axis location used in the following for the investigation conducted on the FFPG will be taken as such. As previously mentioned, despite the fact that an optimal reduced frequency was found during the optimization of the aerodynamic system, its value will not be kept for the following. The reduced frequency is strongly linked with the dynamic of the aeroelastic system due to the resonance of the structure. It is thus important to keep it as a variable for now (i.e. its value will be fixed together with the parameters related to the structural system).

8 Aeroelastic Modeling of a Flapping Foil Power Generator

The objective of this section is to develop an aeroelastic model of a semi-active Flapping Airfoil Power Generator. For this type of system, only the pitching motion is prescribed by a control law. The energy is thus extracted through the plunging motion and the use of a damper for instance.

8.1 Structural Model

8.1.1 System Properties

The structural system is assumed to be composed of a foil linked to a fixed body by a spring of stiffness K_h . The energy extraction is performed on the heaving axis with a proportional damping C_h . No stiffness and no damping is considered on the pitching axis. However, since a semi-active system is investigated, the pitching motion will be prescribed by a controller. Figure 18 shows a sketch of the structural model considered for the semi-active Flapping Foil Power Generator.

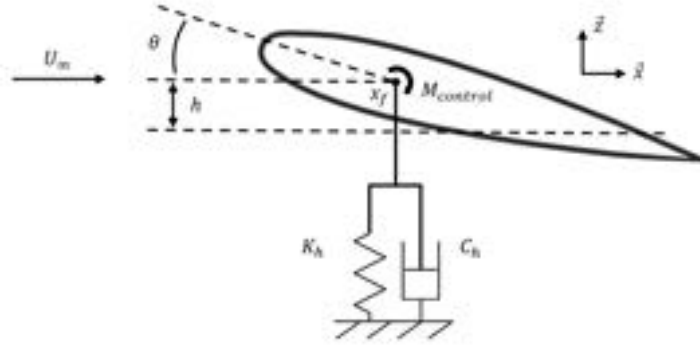


Figure 18: Sketch of the Structural Model considered for the Semi-Active Flapping Foil Power Generator.

The aerodynamics characteristics defined previously have been kept the same. The Reynolds is kept at $Re = 1.7 \times 10^5$, this corresponds to a chord of $c = 0.25$ m and a freestream velocity of $U_\infty = 10.0$ m.s⁻¹. The airfoil NACA0012 was also conserved for the following analysis.

The system has been defined for a span equal to $b = 1$ m. All the results obtained will be thus expressed by meter span. This will allow to scale the FFPG very easily in the spanwise direction. The 3D aerodynamic effects are, by consequence, neglected by this approach. LDVM is only providing the aerodynamics forces acting on a two-dimensional airfoil.

To obtain the value of the mass and of the inertia associated to this system, a material needs to be selected. Carbon fiber reinforced polymers (CFRP) appears as the most straightforward choice motivated by its lightness and his strength compared to other type of material. CFRP composites can be up to 10 times stronger and 5 times lighter than steel as mentioned in [37]. The characteristics of this material were taken from [37]. A CAD (Computer-aided design) of the current system has been setup and allowed an estimation of the mass per unit span of the current foil section. The values are provided in Table 3. The authors point out that the mentioned mass corresponds to an unitary span of a hollow wing with a skin thickness of 2.5 mm.

Regarding the damping on the heaving axis, it appears as the main source of energy extraction for a semi-active system. A proportional damping C_h have been considered, meaning that the resultant damping force is directly proportional to the velocity of the system \dot{h} .

For the current aeroelastic study, some parameters need to be fixed to limit the search space. One can recall that the most optimal parameters/kinematics under an aerodynamic point of view have been obtained previously. Thus, the most optimal value obtained for the pitching amplitude and the rotational axis will be taken equal to their aforementioned values. Among the parameters already investigated for the aerodynamical system, the reduced frequency will be still considered as a variable for the aeroelastic study. The frequency appears as a driven parameter in such system because of its ability to excite the system, which might lead to larger heaving amplitude and thus more energy extraction. The reduced frequency is here refereed as the reduced frequency of the prescribed pitching motion.

| Parameters | Values |
|------------|-------------------------|
| m | 1.9 kg.m^{-1} |
| U_∞ | 10.0 m.s^{-1} |
| c | 0.25 m |
| θ_0 | 79.5° |
| x_f/c | 0.32 |

Table 3: Parameters fixed for the current Aeroelastic Analysis.

The objective is here to find the most optimal coupling between the values of damping C_h and stiffness K_h with a reduced frequency k which would maximize the energy output. Table 4 shows the search space which will be investigated for these parameters.

| Parameters | Range |
|------------|---------------------------------|
| C_h | $0.5 - 40.0 \text{ N.s.m}^{-2}$ |
| K_h | $5.0 - 5000.0 \text{ N.m}^{-2}$ |
| k | $0.15 - 0.63$ |

Table 4: Search Space for the current Aeroelastic Analysis.

8.1.2 Governing equations

A simple two-dimensional flat plate with two degrees of freedom is considered. Some angles will be used in the following and a brief description is provided. θ corresponds to the angle between the flat plate and the frame of reference and α is the angle of attack. m refers to the mass of the flat plate (expressed by unit span) and c to its chord. x_g is the position of the center of gravity, which is assumed to be at mid-chord (uniform mass). The system is assumed to rotate around an axis associated to a location x_f . x_g and x_f are expressed from the leading edge of the flat plate.

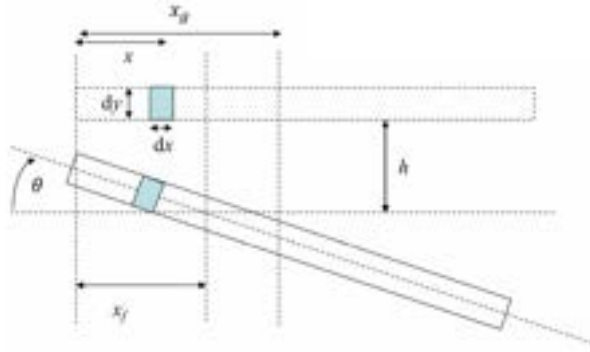


Figure 19: Sketch of the integration performed for the derivation of the kinetic energy T .

One way of deriving the equations that describe the structural system considered is to estimate the velocity of a point M on the flat plate presented in Figure 19. Then, the kinetic energy of the system can be computed with equation (17). For the integration, a linear density ρ is used, the system is assumed to have a uniform mass.

$$T = \frac{1}{2} \int (\vec{V}_M)^2 dm = \frac{1}{2} \left(\dot{h} + (x - x_f) \dot{\theta} \right)^2 dm \quad (17)$$

$$dm = \rho dr \quad (18)$$

After integrating the squared velocity, the kinetic energy can be recast into Equation (19), where some coefficient can be identified. I_θ is the moment of inertia associated to the system. $S_{h\theta}$ represents the coupling term between the momentum equation and the motion of the structural system on the axis \vec{z} .

$$T = \frac{1}{2} m \dot{y}^2 + \dot{h} \dot{\theta} [m (\frac{c}{2} - x_f)] + \frac{1}{2} m \left(\frac{c^2}{3} - c x_f + x_f^2 \right) \dot{\theta}^2 \quad (19)$$

$$S_{h\theta} = m \left(\frac{c}{2} - x_f \right), \quad I_\theta = m \left(\frac{c^2}{3} - c x_f + x_f^2 \right) \quad (20)$$

By using Lagrange equations, it is possible to derive the equations of motion driving the current structural system. These equations are presented in (21) for the equation on \vec{z} and in (22) for the equation on \vec{y} .

$$m\ddot{h} + S_{h\theta}\ddot{\theta} + C_h\dot{h} + K_h h = F_h \quad (21)$$

$$I_\theta \ddot{\theta} + S_{h\theta} \ddot{h} = M_\theta + M_{\text{control}} \quad (22)$$

In the current approach, a semi-active system is investigated. The motion along the plunge axis is assumed to be free. The damping term is the source of the energy extraction in this case. Only the pitching movement is prescribed and thus controlled by a controller. M_{control} represents the action of the controller. F_h and M_θ represent the aerodynamical loads.

The previous equations need to be solved. It is convenient to use the state-space formalism for that. The mass matrix M , the stiffness matrix K and damping matrix C are presented in (23). The state vector \vec{X} is defined to include the positions h , and the θ angle. The first derivatives of the previous variables are also included in the state vector \vec{X} .

$$M = \begin{pmatrix} 1 & 0 & 0 & 0 \\ 0 & m & 0 & S_{h\theta} \\ 0 & 0 & 1 & 0 \\ 0 & S_{h\theta} & 0 & I_\theta \end{pmatrix} ; \quad C = \begin{pmatrix} 0 & 0 & 0 & 0 \\ 0 & C_h & 0 & 0 \\ 0 & 0 & 0 & 0 \\ 0 & 0 & 0 & C_\theta \end{pmatrix} ; \quad K = \begin{pmatrix} 0 & 0 & 0 & 0 \\ K_h & 0 & 0 & 0 \\ 0 & 0 & 0 & 0 \\ 0 & 0 & K_\theta & 0 \end{pmatrix} \quad (23)$$

$$D = \begin{pmatrix} 0 & 1 & 0 & 0 \\ 0 & 0 & 0 & 0 \\ 0 & 0 & 0 & 1 \\ 0 & 0 & 0 & 0 \end{pmatrix} \quad (24)$$

The final system of ordinary differential equations to solve is provided by equation (25). The problem derived here is an initial value problem, and to integrate it given an initial state, an explicit Runge-Kutta method of order 5 is used. The *SciPy* implementation of such a solver has been used [38].

$$\begin{bmatrix} \dot{h} \\ \ddot{h} \\ \dot{\theta} \\ \ddot{\theta} \end{bmatrix} = M^{-1} \left(-K - C + D \right) \begin{bmatrix} h \\ \dot{h} \\ \theta \\ \dot{\theta} \end{bmatrix} + M^{-1} \begin{bmatrix} 0 \\ F_h \\ 0 \\ M_\theta + M_{\text{control}} \end{bmatrix} \quad (25)$$

8.2 Control Strategy

As mentioned previously, the pitching motion needs to be controlled in a semi-active system. For this purpose, a PID controller has been implemented. The reference motion is defined as a sinusoidal variation of the pitching angle θ . This control problem being not too challenging, a basic PID controller has been shown sufficient. The PID controller has three types of gains: the proportional gain K_p , the integral gain K_i and the derivative gain K_d .

The calibration of the PID was done visually by assessing how the reference pitching motion was followed (time response, delay, etc.). Further investigations on the characteristics of the controller are expected to prove the efficiency of the control.

The main challenge that was encountered when calibrating the controller (i.e. finding the right combination of gains) was the variation of frequency in the kinematics investigated. Changes in frequency are modifying the responsiveness of the controller which is difficult to manage. However, parametric analysis and multi-objectives optimizations of the current system are expected, thus the gains of the controller have been fixed to values providing satisfactory results for the range of frequency sought (Tab. 5).

| Parameters | Value |
|------------|---|
| K_p | 500.0 N.rad ⁻¹ |
| K_i | 75.0 N.rad ⁻¹ .s ⁻¹ |
| K_d | 10.0 N.s.rad ⁻¹ |

Table 5: Gains of the PID controller applied on the pitching motion.

8.3 Coupling between Structural and Aerodynamical Models

An aeroelastic model contains usually a structural model and an aerodynamical model (with or without control). A neural network has been developed to predict the aerodynamical forces applied on a FFPG given its states. The neural network has to be seen as the aerodynamical model in the current approach to develop an aeroelastic model. This neural network has been trained on a dataset generated by LDVM. Further information on the training/validation and test procedures have been mentioned previously. The use of the neural network is here mandatory since coupling between LDVM (Fortran script) and the structural system would not have been possible.

The aerodynamic forces will thus be modeled in the same way in the aeroelastic problem. The neural network will provide F_h and M_θ in equation (25). The fact that the neural network is coupled with the structural system complicates the way the equation are solved. As mentioned previously, an explicit Runge-Kutta method of order 5 is used. However, this method does not use a fixed time stepping to solve the equations and the neural network takes as input the states of the system at fixed time steps. The tolerances used by the solver have thus been set to infinity and a maximal time step have been used. This contributes to a loss of accuracy when solving the equation, but this loss is assumed to be negligible to the following of the analysis. The right way of tackling this problem is obviously to change the solver.

One should remember that initially, to build the neural network and to decrease the size of the problem (i.e. size of the dataset and size of the neural network), the heaving amplitude has been fixed to $h_0/c = 0.5$. The frequency k , the rotational axis location x_f and the pitching amplitude θ_0 were still allowed to vary. This means that the neural network have been trained to predict aerodynamic forces only for sinusoidal motions with heaving amplitudes of $h_0/c = 0.5$. However, nothing is constraining the system to effectively oscillate with the already mentioned heaving amplitude. In reality, it is the combination of damping C_h , stiffness K_h and reduced frequency k (for the prescribed pitching motion) which would define the oscillatory characteristics of the heaving of the semi-active system.

If one is interested in a parametric analysis between the values of damping C_h , stiffness K_h and reduced frequency k , for some combination of values, the resulting heaving amplitudes may be outside the initial training dataset of the neural network. This would results in a wrong prediction of the aerodynamic forces (lift and moment). However, even for cases outside the training dataset, it is not clear that the neural network would not predict the forces correctly since the neural network is based on the states of the system ($[h, \dot{h}, \theta, \dot{\theta}, \dots]$). For a case outside the training sequence, the neural network might nevertheless contain a similar state (including perhaps other kinematics) and thus predict something that is not completely wrong.

In the current approach, the only way to identify any discrepancies between the neural network predictions and what should be its predictions based on the motion imposed by the structural system is to solve the motion for a given set of parameters with the neural network. The resulting motion could be then used as an input for LDVM to generate the "true" aerodynamic forces corresponding to that motion. Lastly, a comparison between the loads generated by LDVM and by the neural network could be made for quantitatively assessing the error corresponding to that motion. The set of parameters used for this analysis is the following: $\{k = 0.462, C_h = 15.877 \text{ N.s.m}^{-2}, K_h = 2500.0 \text{ N.m}^{-2}\}$. Figure 22a shows a clear difference between the predictions of the neural network and the output of LDVM (i.e. the predictions that should have been obtained with the neural network) given the motion induced by the structural system.

One can notice that the heaving amplitude induced by the structural system is higher than $h/c > 1.0$ which is clearly outside the dataset used to train the neural network. Another way of describing the situation would be to say that the neural network is not able to predict accurately the aerodynamic forces given the states ($[h, \dot{h}, \theta, \dot{\theta}, \dots]$) associated to the motion of the system. A wrong prediction of the forces acting on the system results obviously in a wrong prediction of the motion and thus of the power extracted by such a system.

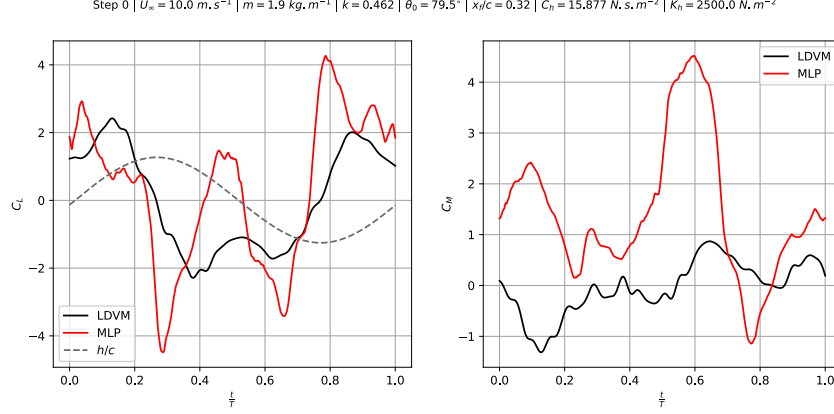


Figure 20: Lift Coefficient C_L and Moment Coefficient C_M predicted by the neural network for the motion induced by the structural system. Comparison with the output from LDVM for the corresponding kinematic.

8.4 Active Learning

A way of tackling this problem could be to use an active learning strategy. In an iterative manner, the neural network coupled with the structural system would be used to solve the kinematics of the system in a first time. Then, these kinematics could be used to retrain/fine-tune the neural network to predict accurately the forces corresponding to these motions. After some iterations, which will be called "steps" in the following, a convergence should be reached between prediction of the neural network and the LDVM outputs. This is the main interest behind using active learning. This can also be applied to parametric analysis and optimizations, after some steps the results should converge towards the same value, which will be assumed as accurate because similar to LDVM outputs (i.e. reference used in this study for the prediction of aerodynamic forces, its limitations have been mentioned previously). An Active Learning procedure has been used and its principle is illustrated in Figure 21.

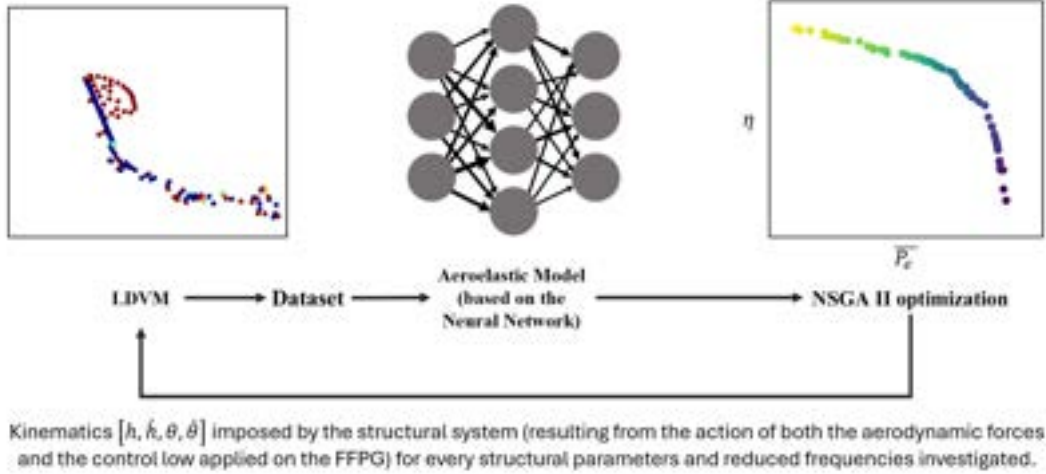


Figure 21: Complete framework used to converge on an accurate aeroelastic model of a Flapping Foil Power Generator, involving the training of a neural network through an active learning approach to provide predictions of the Pareto front by the NSGA II algorithm.

For each step of this active learning procedure, a new dataset is generated. The neural network of the previous step is coupled with the structural system to obtain the kinematics corresponding to cases included in the search space. An equally spaced tridimensional grid of this search space is defined. When the kinematics of all the points of this search space are extracted, there are given as input to LDVM to predict the corresponding forces. The new dataset will contain the new association between states and aerodynamic forces (i.e. $[h, \dot{h}, \theta, \dot{\theta}, \dots]$ and $[C_L, C_M]$).

The neural network is fine-tuned in the same way as previously mentioned for the settings associated to the training. However, a reduced number of epoch is used ($N = 25$) because it can be observed that the validation loss reaches its plateau faster than for the initial training.

Figure 22 shows the comparison between the neural network predictions and the LDVM outputs for the following case: $\{k = 0.462, C_h = 15.877 \text{ N.s.m}^{-2}, K_h = 2500.0 \text{ N.m}^{-2}\}$ at each step of this active learning procedure. The main observation is that the active learning seems to converge quite rapidly. As mentioned before, for step 0 (Fig. 22a), the neural network is not predicting satisfactory results as it was expected. However, from step 1 to step 5 the neural network predictions are slightly evolving for this specific case (Figs. 22b, 22c, 22d, 22e and 22f). This seems to indicate convergence on the active learning procedure, even if this observation is local and might not be the case for the whole search space.

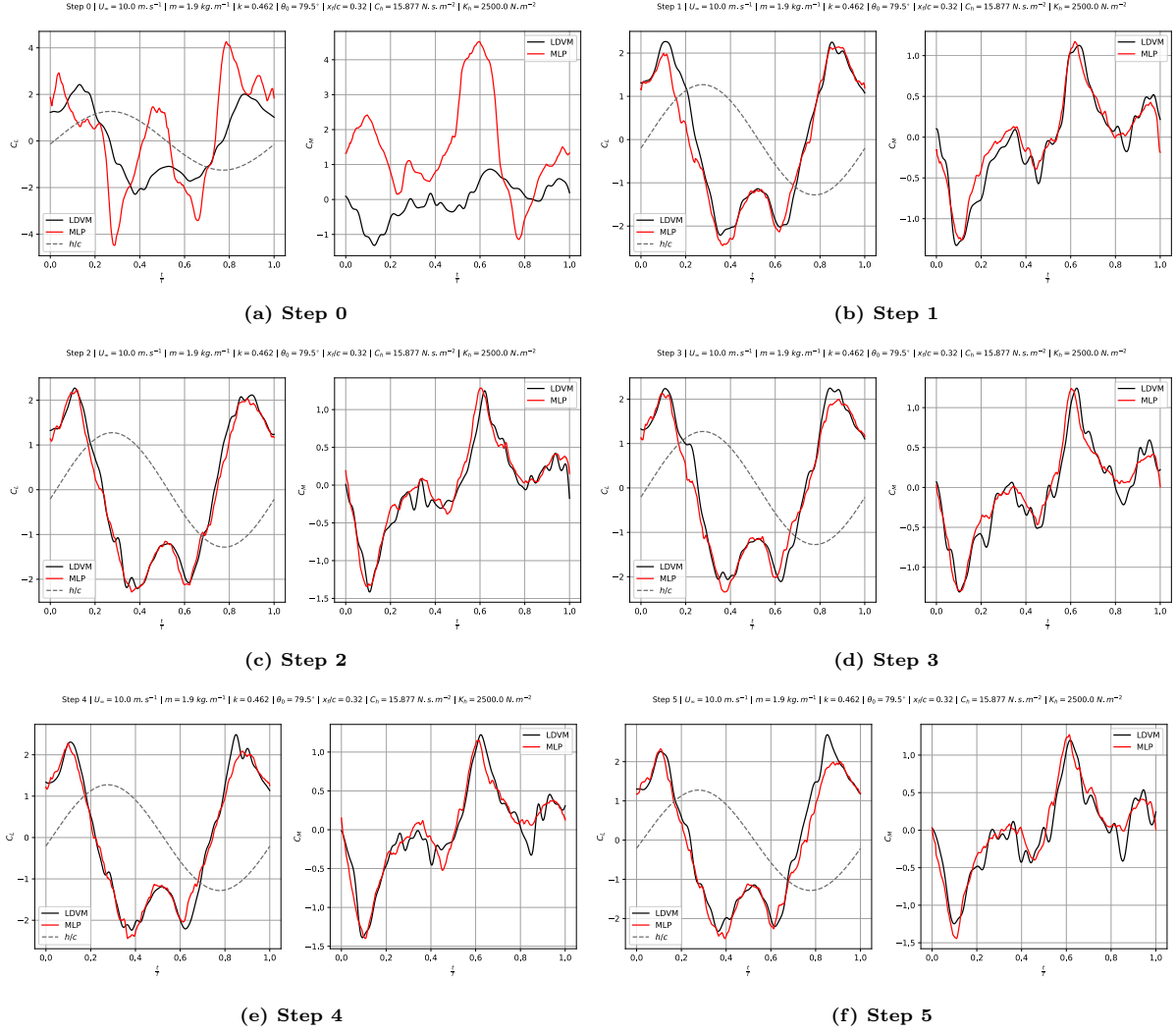


Figure 22: Lift Coefficient C_L and Moment Coefficient C_M predicted by the neural network for the motion imposed by the structural system. Comparison with the output from LDVM for the corresponding kinematics.

8.5 Parametric Analysis

A parametric analysis have been conducted at each step on the efficiency of the FFPG. The efficiencies of the system have been evaluated at every point of the uniformly spaced tridimensional grid which represents the search space. Figure 23 and 24 show the results of this parametric analysis at only two reduced frequency for plotting purposes even if the whole range of the search space has been covered. A GIF animation of this parametric study can be found on the Git repository of this study.

It is worth to note that the evaluation of a single case requires a computational time of the order of 30 seconds. To be able to obtain the following plots, the uniformly spaced tridimensional grid which represents the search space contains $15 (k) \times 25 (C_h) \times 50 (K_h) = 18750$ points. One can clearly see that the computational time to obtain this parametric study with a sequential execution of the evaluations is of the order of a week. This was tackled with the use of parallel programming running on supercomputers. Parametric studies where all the evaluations conducted are independent of the others are relatively easy

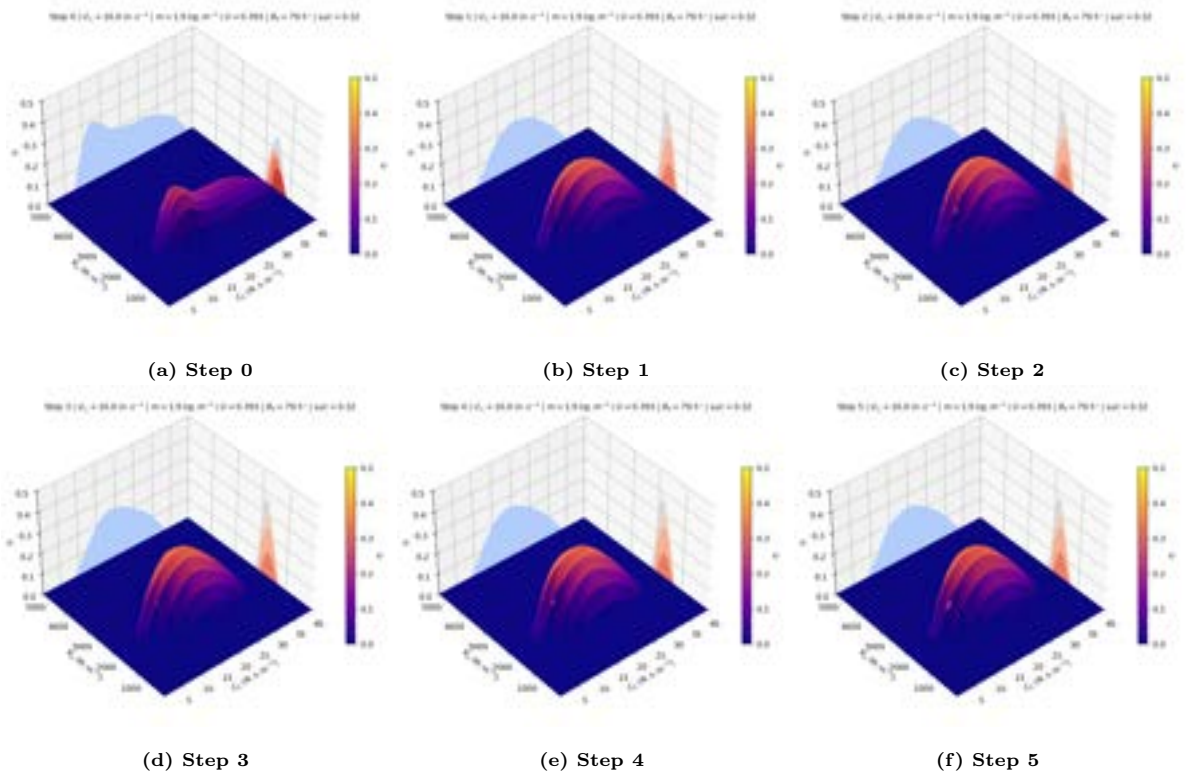


Figure 23: Parametric Analysis on the efficiency η depending on the damping C_h and the stiffness K_h . Reduced frequency $k = 0.393$. Negative efficiencies have been set to 0 for plotting purposes.

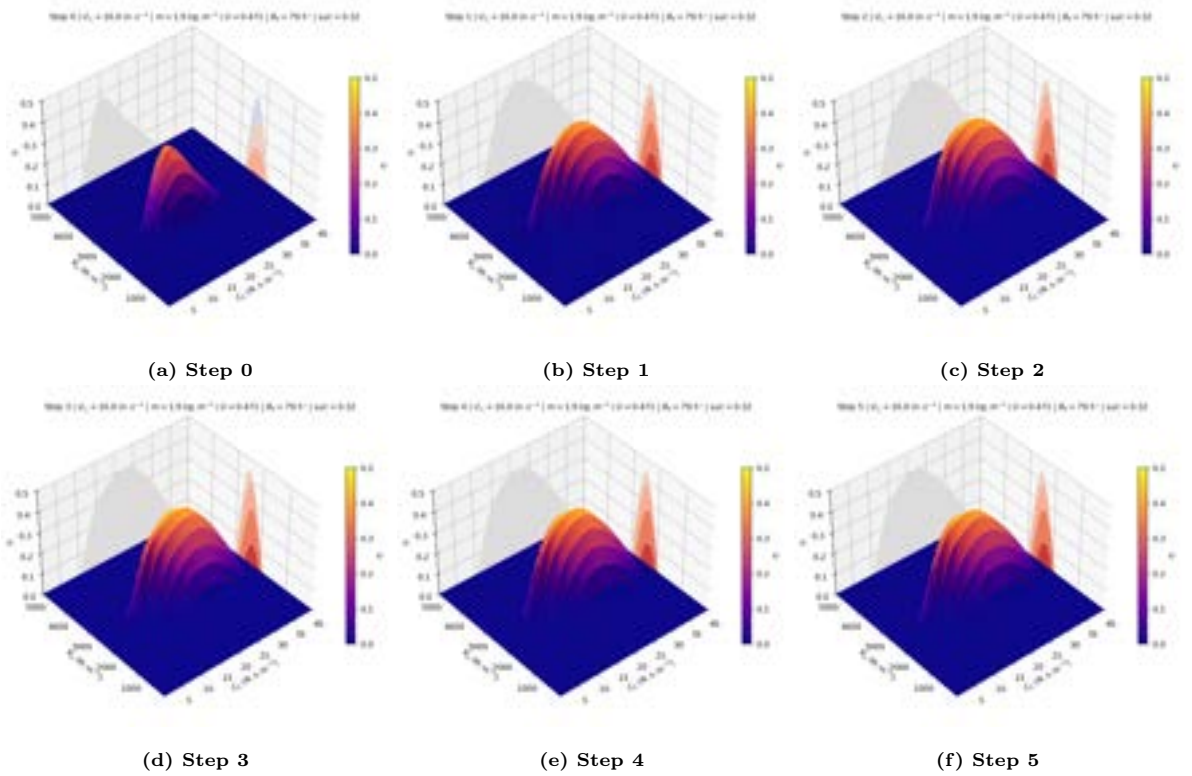


Figure 24: Parametric Analysis on the efficiency η depending on the damping C_h and the stiffness K_h . Reduced frequency $k = 0.471$. Negative efficiencies have been set to 0 for plotting purposes.

to parallelize. In fact, full parallelization can be achieved since all the evaluations are independent. The MPI (Message Passing Interface) library [34] has been used. With 4 nodes (*CPU Intel Xeon E5-2670v3*,

24 cores, 64 Go RAM), the time to obtain this parametric study is reduced to approximately 1 hour and 30 minutes, making this analysis possible.

One can notice the clear difference between the step 0 (Fig. 23a and 24a) for which the active learning was not performed and the other steps (Figs. 23b - 23f and Figs. 24b - 24f). The local observation conducted previously for an unique point in the search space can now be generalized. In an iterative manner, the active learning converges towards a neural network which once coupled with the structural system is predicting aerodynamical forces (and thus kinematics) that are matching to what LDVM would have provided for the corresponding kinematics.

Another important observation from this parametric study is the range of the variables that are associated to high efficiency for the power extraction. This information allows to reduce the search space investigated for a further optimization. Some combinations of parameters are not relevant (i.e. they could lead to very low efficiency, even negative values sometimes) and should not be considered by the optimization algorithm. This parametric study is here used to define the search space which will be considered for the following optimization.

In Figure 25, the same parametric analysis has been conducted for multiple reduced frequencies by considering the neural network obtained at the last step (step 5) of the active learning process. One can identify that a reduced frequency $k < 0.23$ and $k > 0.628$ would lead to a low value for the maximal efficiency that could be reached in the search space of damping C_h and stiffness K_h . The maximum efficiency that can be reached seems to lie between $k < 0.471$ and $k < 0.550$. The same approach can be used to identify the most relevant search space for the following optimization, presented in Table 6.

| Parameters | Range |
|------------|----------------------------------|
| C_h | 5.0 – 30.0 N.s.m ⁻² |
| K_h | 500.0 – 5000.0 N.m ⁻² |
| k | 0.236 – 0.628 |

Table 6: Optimal Search Space for Multi-Objectives Optimization based on the current Parametric Analysis.

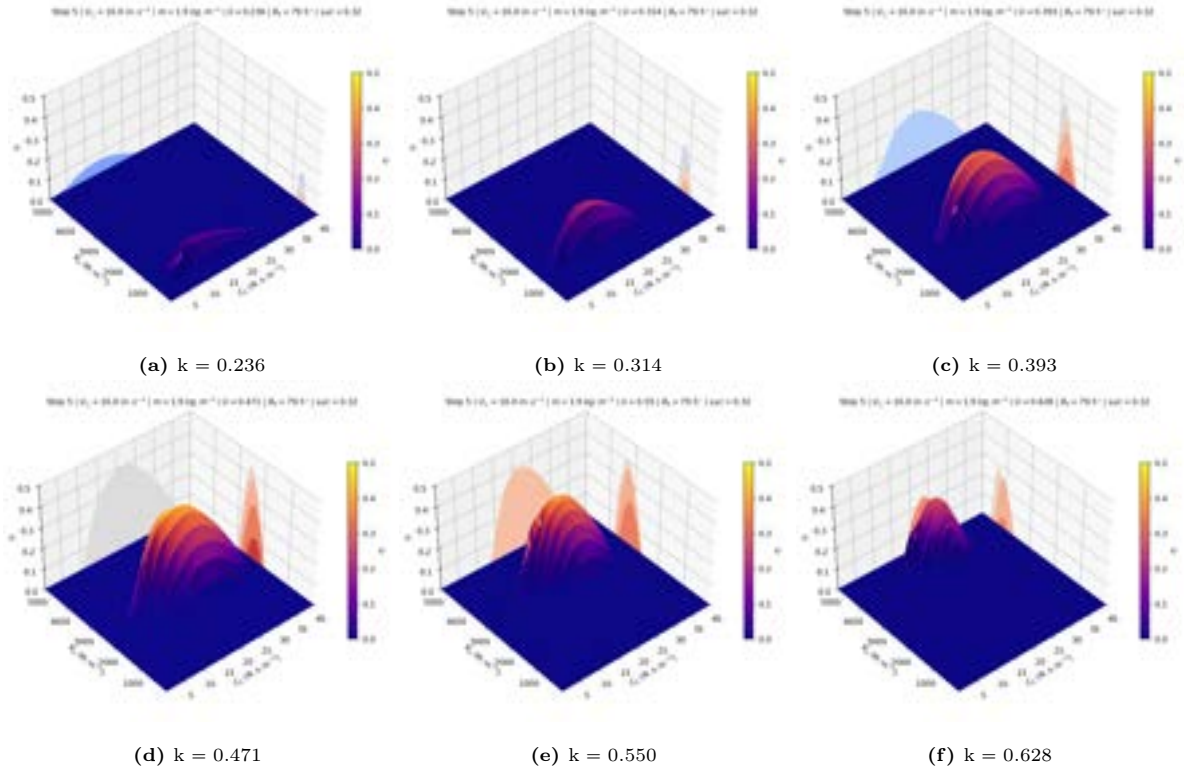


Figure 25: Parametric Analysis on the efficiency η depending on the damping C_h and the stiffness K_h . Step 5 of the active learning process and variable reduced frequency k . Negative efficiencies have been set to 0 for plotting purposes.

8.6 Multi-Objectives Optimization

The objective of the current study is to identify the combination of values for the damping C_h , the stiffness K_h and the reduced frequency k associated to the pitching controlled motion which leads to an optimal energy extraction. The previous parametric analysis allowed to define the relevant search space to consider for this optimization problem. Now, the optimization problem needs to be formalized to be able to implement it.

What was defined before as "an optimal energy extraction", can be seen in two ways. The most straightforward way of formulating this idea is to optimize the efficiency η , which is the net power extracted $P_e = P_h + P_\theta$ (with $P_\theta < 0$) divided by the available power in the flow associated to the swept area P_{flow} . Optimizing the efficiency would thus provide the system which allows to extract the maximal power while minimizing the swept area by the foil. In some situation, one could consider that the swept area is not the primary parameter to optimize, the space occupied by the foil not being a concern and that only the power extracted P_e should be maximized. This might result in lower efficiency but higher power extracted P_e with a larger area swept by the foil.

The following multi-objectives optimization problem has been defined:

$$\begin{cases} S = [0.236, 0.628] \times [5.0 \text{ N.s.m}^{-2}, 30.0 \text{ N.s.m}^{-2}] \times [500.0 \text{ N.m}^{-2}, 5000.0 \text{ N.m}^{-2}] \\ x = \{k, C_h, K_h\} \text{ with } x \in S \end{cases} \quad (26)$$

$$\begin{cases} \underset{x \in S}{\text{minimize}} & -\eta(x) \\ \underset{x \in S}{\text{minimize}} & -P_e(x) \\ \text{s.t.} & |P_c| - |P_e| < 0 \end{cases} \quad (27)$$

A constraint was nevertheless applied as depicted above in equation 27 to ensure that the absolute value of the power extracted P_e is greater than the absolute value of the power consumed P_c for the control of the pitching motion.

The neural network and the structural system are coupled with a genetic algorithm for optimization. The implementation of the *NSGA II* algorithm, described by Deb et al. (2002) [39], is used with the Pymoo library [36]. Genetic algorithms are based on the survival of the fittest principle: like in natural evolution, the fittest individuals live through the generations. The stochastic nature of the genetic algorithm makes them suitable in evading local optima, which are typically encountered in such non-convex optimization problems. The *NSGA II* algorithm has proven to be efficient in predicting Pareto fronts in fluid mechanics, and has already been coupled to neural networks, as proposed by Krüger et al. (2022) [40] to optimize the combustion chamber of a rocket engine. For each generation of the algorithm, a mating pool is formed by selecting individuals from the previous generation population. These individuals then go through mutation and cross-over to form offsprings. The offsprings and the previous population are gathered and the new population is created by non-dominated sorting, and finally by crowded distance sorting.

Each individual is composed of the three parameters $[k, C_h, K_h]$. The bounds of the search space are defined in Table 6 and in equation (26). The population is composed of 100 individuals and 50 offspring are generated for each generation. In the present study, the cross-over method is the simulated binary cross-over, and the mutation method is the polynomial mutation (further details can be obtained from [36]).

As mentioned previously, the evaluation of a single case requires a computational time of the order of 30 seconds. Performing this multi-objectives optimization without the use of parallel computing would be extremely long, one might thus think about parallel computing. However, a multi-objective optimization problem with genetic algorithms is not straightforward to parallelize. There is a dependence between one generation and the next one, making the parallelization of the tasks possible but only within one generation. To tackle this complexity, the Dask library [41] coupled to Pymoo [36] has been used. Dask allows the distribution of the evaluation function to a couple of workers and can also be used with MPI [34] which handle distributed memory architecture like the supercomputers. 2 nodes (*CPU Intel Xeon E5-2670v3, 24 cores, 64 Go RAM*) allow to conduct this multi-objectives optimization with a reasonable amount of time, in approximately 1 hour and 10 minutes.

Figure 26 shows the results of the multi-objectives optimization for different steps of the active learning procedure. One can see that the multi-optimization of both the efficiency η and the power extracted

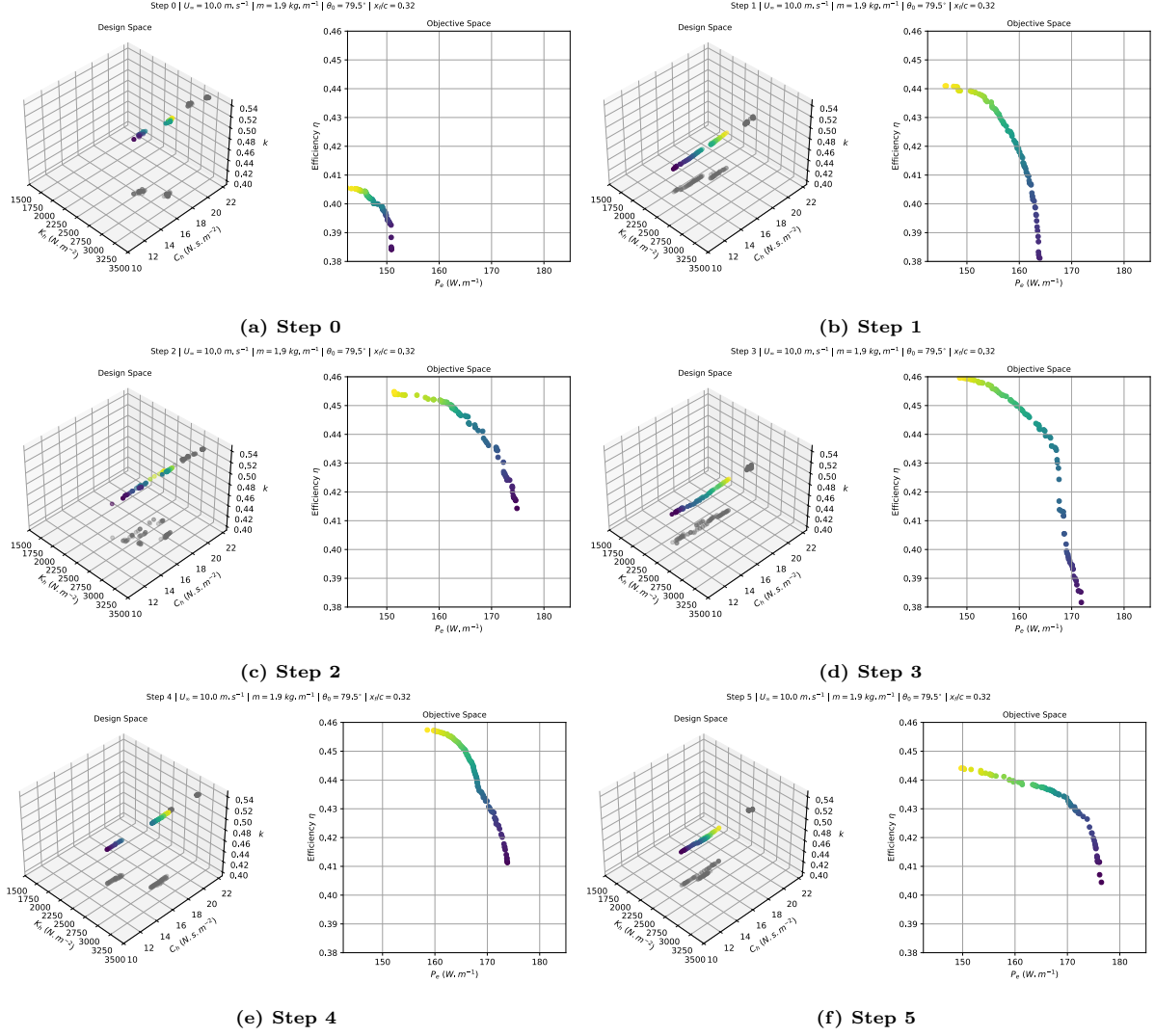


Figure 26: Multi-Objectives Optimization of a Flapping Foil Power Generator (FFPG) with Genetic Algorithm (NSAG2).

P_e lead to the formation of a Pareto front for every steps. On the left extremity of the objective space, one can identify the configuration providing the maximal efficiency η and on the right, the configuration maximizing the energy extracted P_e . The design spaces associated to the objective spaces are also included in Figure 26. The relation between these two spaces is shown by the color-map (colored dots) which allows to link the efficiency η and the power extracted P_e to a specific configuration and vice-versa. One can consider that these design spaces are containing the most optimal configurations possible for the Flapping Foil Power Generator according to the genetic algorithm used.

One can extract the objective spaces obtained for each step of the active learning and plot them in the same figure. This is displayed in Figure 27. All the Pareto front seems to converge after the first two active learning steps, this reveals a convergence of the genetic algorithm. It is true that the Pareto fronts are not completely superimposed (Fig. 27) from step 2 to step 5. However, they are still quite close compared to the gap between step 0 and the other steps. These dependencies between the Pareto front of the last steps could be explained in the following way. Even if the active learning has converged, all the numerical tools used to solve this problem (solver, neural network, etc.) might lead to an estimation of the efficiency η and of the power extracted P_e which slightly differs from one step to another due to the complexity and the number of the tools used.

In order to take that into account, an average of the Pareto fronts corresponding to step 2 to 5 has been made and uncertainty errors of $\pm 1.0\%$ on the evaluation of the efficiency and of $\pm 4 \text{ W.m}^{-1}$ for the power extracted P_e have been set up. This leads to an uncertainty region around the mean of the converged Pareto fronts shown in Figure 27. It is worth to note that all the converged Pareto fronts are included in

this region.

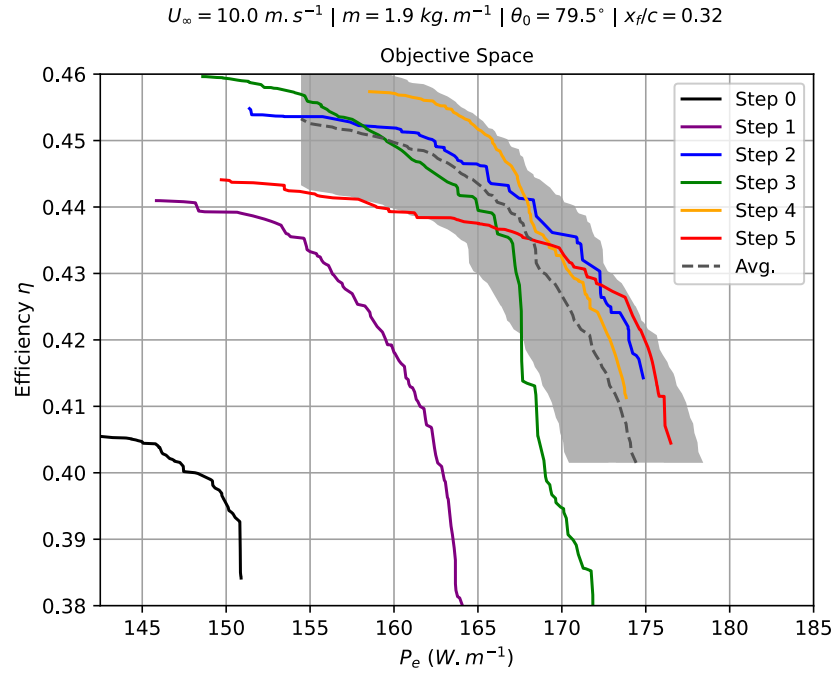


Figure 27: Objective Spaces obtained for each step of the Active Learning procedure. The Pareto fronts representing the tradeoff between efficiency η and the power extracted P_e can be identified and are converging after step no. 2.

The convergence of the optimization is now clear. The results obtained for the last active learning step (no. 5) will be used for the following analysis of the best configuration linked to the Flapping Foil Power Generator.

9 Analysis of the Optimal Flapping Foil Power Generator

A multi-objective optimization of the Flapping Foil Power Generator was conducted with a genetic algorithm and convergence on the results have been obtained through an active learning procedure. The parameters for this optimization were the reduced frequency k , the damping C_h and the stiffness K_h , both of them acting on the heaving motion. The other characteristics of the system have been mentioned previously.

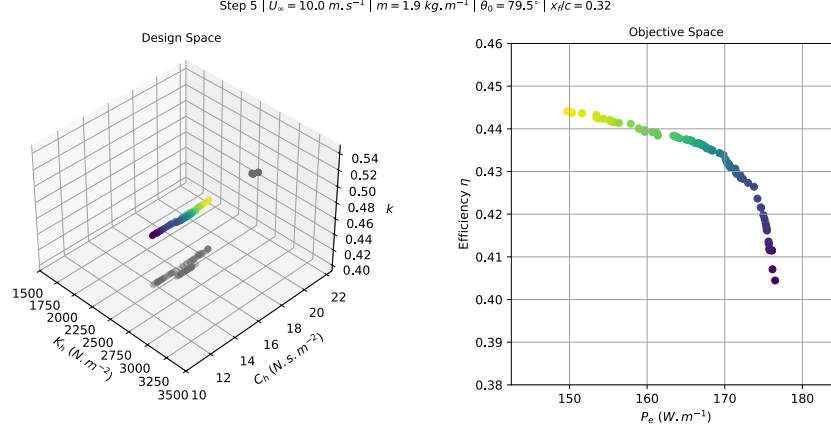


Figure 28: Multi-Objectives Optimization of a Flapping Foil Power Generator (FFPG) with Genetic Algorithm (NSAG2). Results obtained for the last step of the Active Learning procedure (step no. 5).

The optimization corresponding to the last active learning step is recalled in Figure 28. The design space seems to show a direct link between the operating frequency and the stiffness of the system. In fact, there is a one to one relationship between the reduced frequency k and stiffness K_h which leads to maximal energy extraction. This reduced frequency corresponds directly to the natural reduced frequency of the system. If one simplifies the current system by neglecting the pitching motion and the damping on the heaving axis used for energy extraction, the system would become a spring-mass oscillator in this case. The corresponding second order differential equation is shown in equation (28). The good thing about spring-mass systems is that their natural frequency is very easy to obtain analytically, this being provided in equation (29). A quick try with $m = 1.9 \text{ kg.m}^{-1}$ (per meter span) and $K_h = 2500 \text{ N.m}^{-2}$ (per meter span) leads to a reduced frequency of $k = 0.453$ which seems to correspond approximately to the value shown in the design space (Fig. 28).

$$m \ddot{h} + K_h h = 0 \quad (28)$$

$$k = \frac{b}{U_\infty} \sqrt{\frac{K_h}{m}} \quad (29)$$

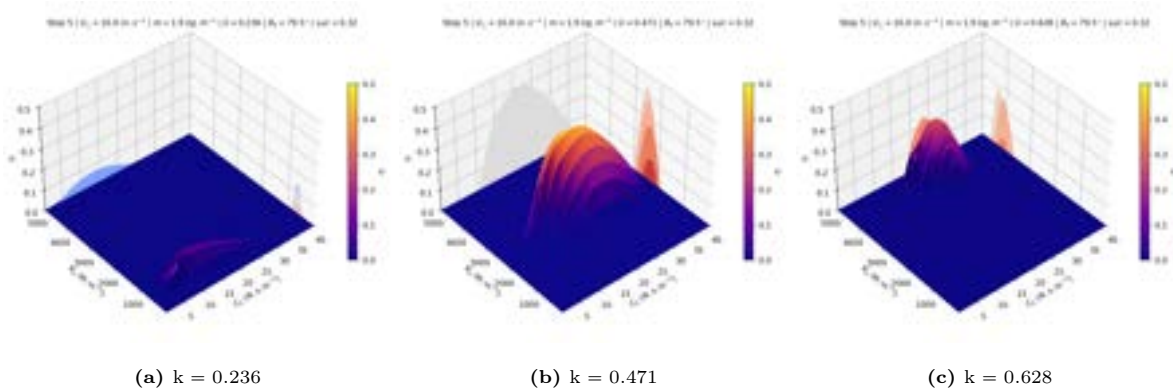


Figure 29: Parametric Analysis on the efficiency η depending on the damping C_h and the stiffness K_h . Step 5 of the active learning process and variable reduced frequency k . Negative efficiencies have been set to 0 for visualization aspects.

The idea of focusing more on the stiffness K_h and the reduced frequency k than on the damping C_h is motivated by the fact that the damping only constrains the amplitude of the motion on the heaving axis.

Larger damping leads to relatively smaller amplitudes (which are associated to higher efficiencies) and smaller damping leads to larger amplitudes (thus associated to lower efficiencies) as shown by the set of solutions provided by the multi-objectives optimization.

However, if the problem was as simple as a mass-spring system, the efficiency of the system would be maximal for all the reduced frequencies and stiffness combinations that correspond to the natural excitation of the system, i.e. a plane in the current design space. In Figures 29a, 29b and 29c, it is possible to see that for the three reduced frequency k considered, the highest efficiency is indeed reached for a stiffness K_h leading to the resonance of the structural system. However, the efficiencies reached for the natural excitation of the FFPG are not the same for the three reduced frequencies. The optimal efficiency (over all the reduced frequencies) is only reached for a specific reduced frequency, which in the current case is the one provided by the optimization.

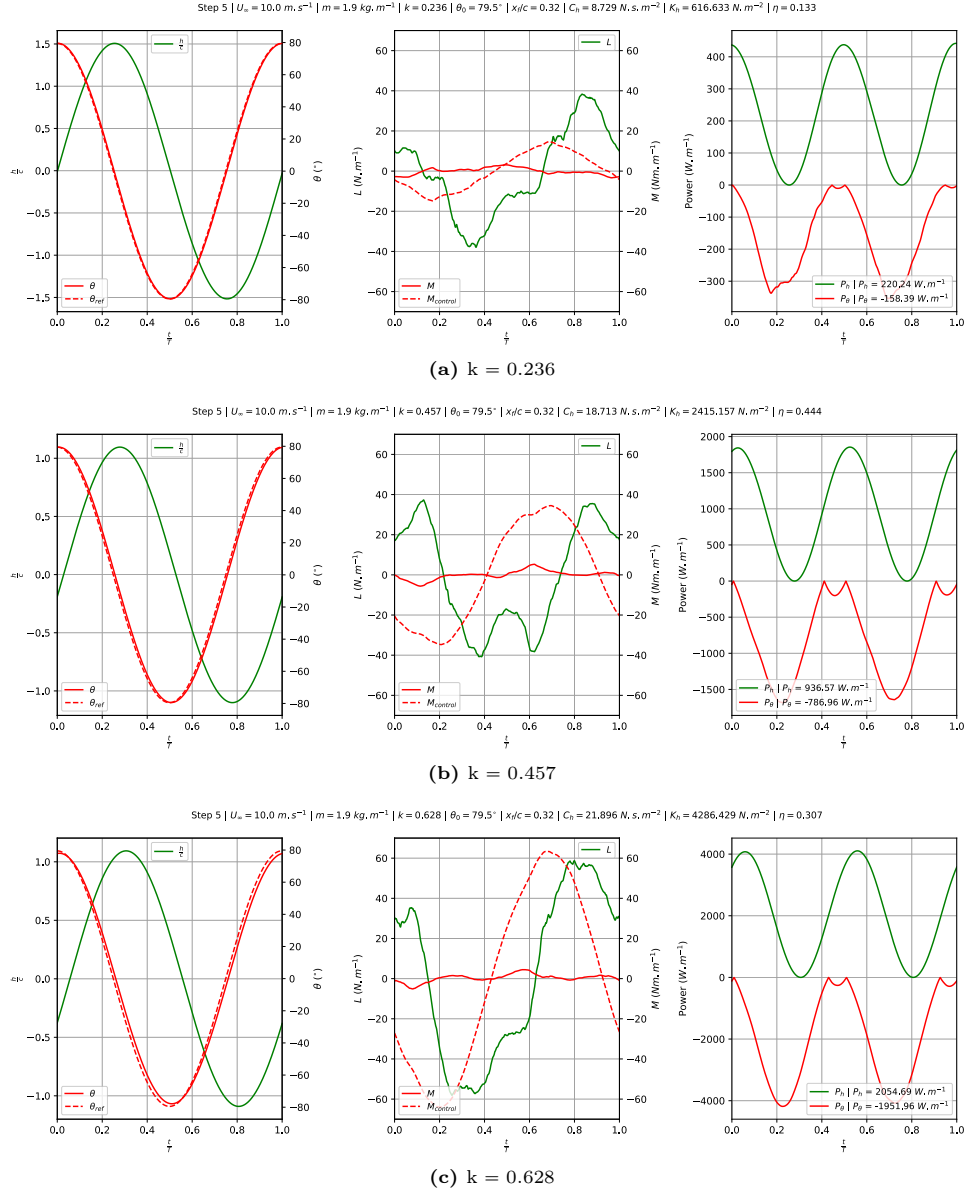


Figure 30: Quantities related to the Flapping Foil Power Generator for different reduced frequencies. The case with $k = 0.457$ (middle) corresponds to the most efficient configuration provided by the multi-objectives optimization performed with *NSGA 2*. For each reduced frequency, the stiffness K_h and damping C_h are designed to induce the natural excitation of the system with a maximal efficiency η .

In order to understand why the maximum efficiency is only reached for a specific reduced frequency, three configurations $\{k, C_h, K_h\}$ leading to the natural excitation of the system (and thus to a local maximal efficiency) will be investigated. The first configuration can be obtained from the optimization previously performed (in Fig. 28), and is described by $\{k = 0.457, C_h = 18.713 \text{ N.s.m}^{-2}, K_h = 2415.157 \text{ N.m}^{-2}\}$

as the most optimal case in term of efficiency ($\eta = 0.444$). For comparison, the stiffness K_h leading to the resonance of the system at $k = 0.236$ and at $k = 0.628$ are considered: $\{k = 0.236, C_h = 8.729 \text{ N.s.m}^{-2}, K_h = 616.632 \text{ N.m}^{-2}\}$, $\{k = 0.628, C_h = 21.896 \text{ N.s.m}^{-2}, K_h = 4286.429 \text{ N.m}^{-2}\}$. These cases are assumed to represent relevant points of comparison because their efficiency (maximal for each reduced frequency) are relatively low ($\eta = 0.133$ for $k = 0.236$ and $\eta = 0.307$ for $k = 0.628$).

All the variables ($h, \theta, C_L, C_M, P_e, P_c$, etc.) associated to these three cases are shown in Figure 30. First, one can see that for all the reduced frequencies, the pitching and heaving motions are very similar, both with a phase shift of 90° between the pitch and the plunge. The amplitudes of the heaving are indeed different but as mentioned previously this is due to the different values of damping used and do not impact the natural excitation of the system (i.e. impact only the amplitude of the resonance, not the reduced frequency and stiffness at which it is happening). The power extracted ($P_h = P_e$ in the case of semi-active FFPG) and the power consumed (here P_θ) are very similar in their shape but not in their amplitude. The difference in amplitude comes from the different reduced frequency considered. For large reduced frequencies, the period of the motion will be smaller and more cycles are performed per second, which will result in higher power extracted and consumed.

The main difference lies in the aerodynamical forces generated on the foil. One can see in Figures 30a ($k = 0.236$), 30b ($k = 0.457$), and 30c ($k = 0.628$), that the behaviors of the vertical forces F_h acting on the system are completely different. The amplitudes are similar between $k = 0.236$ and $k = 0.457$. However for $k = 0.457$, when θ is maximal, the maximum lift generated on the foil seems to act longer than for the corresponding case at $k = 0.236$. It worth to note that the amplitude of the vertical force for $k = 0.628$ is larger than for $k = 0.236$ and $k = 0.457$.

Regarding the pitching moment, the behaviors between $k = 0.236$ and $k = 0.457$ are similar with indeed a control of larger amplitude for $k = 0.457$ due to higher reduced frequency. One can observe that the pitching moment applied by the controller to follow the reduced frequency of $k = 0.628$ for the pitching motion is extremely high. This could lead to higher energy consumption.

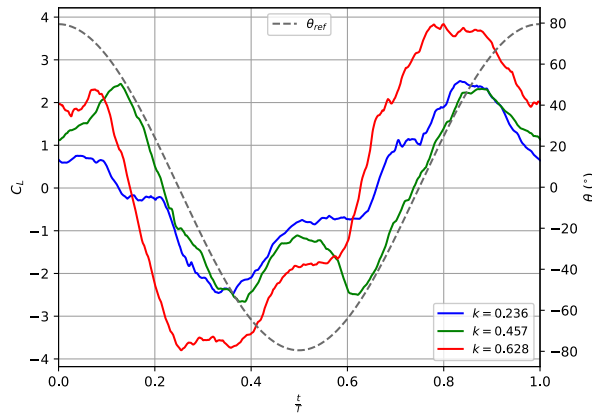


Figure 31: Lift Coefficient C_L generated on the foil for different reduced frequencies k . For each reduced frequency, the stiffness K_h and damping C_h are designed to induce the natural excitation of the system resulting in maximal efficiency η .

The lift coefficient generated on the foil for the three reduced frequencies have been plotted on Figure 31 for better visualization. Snapshots of the vortexes shed from the leading and trailing edges by LDVM have been provided on Figures 32, 33 and 34. Snapshots have been taken at multiple instants during one period.

One can clearly notice that for $k = 0.236$ and $k = 0.457$, between $t/T = 0.25$ and $t/T = 0.5$, when θ increases, a leading edge vortex is shed (Figs. 32c, 33c and 34c) and generates a significant lift force as shown in Figure 31. These leading edge vortexes appear as the manifestation of dynamic stall. Dynamic stall is a non-linear unsteady aerodynamic effect that occurs when airfoils rapidly change the angle of attack. The rapid change can cause a strong vortex to be shed from the leading edge of the airfoil, and travel backwards above the wing. The vortex, containing high-velocity airflow, briefly increases the lift produced by the wing. Corke et al. [42] provide a clear overview of this flow regime. For $k = 0.236$, the effect of leading edge vortex is rapidly reduced by a counter-rotating vortex shed from the trailing edge developing on the suction side of the foil (Fig. 32d). This leads to a lift force which decrease ($t/T = 0.625$) with further reduction of the pitch angle. The initial enhancement in the lift due to

dynamic stall is instantaneously discarded by this counter-rotating trailing edge vortex. The FFPG is thus undergoing a traditional stall which does not improve the lift force generated anymore.

However, for $k = 0.457$, at $t/T = 0.625$, the leading edge vortex is still attached to the foil and keeps generating lift (Fig. 33d). The enhancements due to dynamic stall are not discarded in this case. The foil will smoothly come back in its horizontal position without any vortex shed from the trailing edge. This could explain the difference in efficiency between $k = 0.236$ and $k = 0.457$. The lift generated by this leading edge vortex is the primary source of power, thus reducing it, leads to lower power extraction. Despite the fact that the structural system is in resonance for $k = 0.236$ and $k = 0.457$ (thanks to different values of stiffness and damping) the aerodynamic associated to these two cases is clearly not the same. Corke et al. [42] mentioned that dynamic stall may lead to an eruption of vorticity that organizes into a well-defined dynamic stall vortex and massive fluctuations in aerodynamic loads that can couple with the FFPG structural dynamics.

Regarding the case at $k = 0.628$, in Figure 34d, it seems that the pitching motion is interfering with the leading edge vortex. The foil seems to push the vortex away to be able to follow its reference pitching motion, leading to higher energy consumption to control the pitch. Despite higher lift generation, the moment required to follow the pitching motion could induce higher energy consumption which may decrease the efficiency of this specific case.

In order to conclude this brief analysis, only one reduced frequency allows to maximize the dynamic stall effects. The reduced frequency of the pitching motion must be such that the vortex generated at the leading edge stays as long as possible on the suction side of the foil. This observation may be represented by a relation between the reduced frequency and the convection velocity of the leading edge vortex. Green et al. [43] conducted measurements on the convection velocity of dynamic stall vortices. Given the range of reduced pitch rate $r = b\dot{\theta}/U_\infty$ investigated in the current study and based on the measurement from Green et al. [43], a convection velocity of $U_c/U_\infty \approx 0.3$ was considered. From the visualization of the most optimal case (Figs. 33c, 33d, 33e), the leading edge vortex should travels approximately a semi-chord per quarter period. This statement, which is formulated in equation (30), ensures to fully benefit from the increase in lift provided by the dynamic stall. One can show that equation (30), leads approximately to the reduced frequency provided by the multi-objectives optimization, which is $k = 0.457$.

$$k = \frac{\pi}{2} \left(\frac{U_c}{U_\infty} \right) = (0.3) \frac{\pi}{2} = 0.47 \quad (30)$$

Equation 30 may not reflect exactly the reality due to its simplicity but might be used as preliminary assessment of the reduced frequency which should be considered when designing such FFPG. Knowing that the optimal FFPG are obtained for the natural excitation of the system, the right stiffness K_h can be obtained with equation (29) from the reduced frequency found just before with equation 30. The other parameters should be adjusted afterwards, based on the aforementioned reduced frequency k and stiffness K_h that are shown to drive the designs of such FFPG.

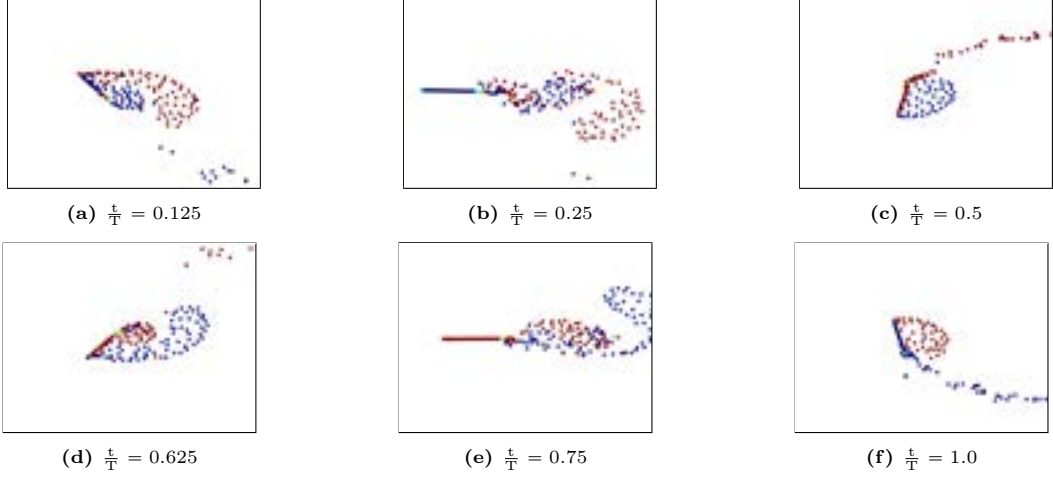


Figure 32: Visualization of the vortices shed from the leading and trailing edges by LDVM. The natural excitation of the FPG associated to $k = 0.236$ is shown.

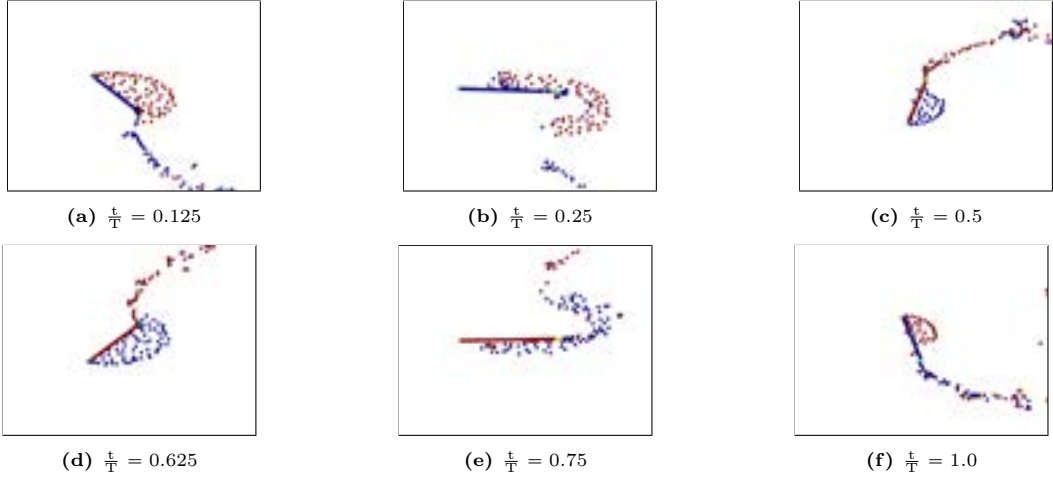


Figure 33: Visualization of the vortices shed from the leading and trailing edges by LDVM. The natural excitation of the FPG associated to $k = 0.457$ is shown.

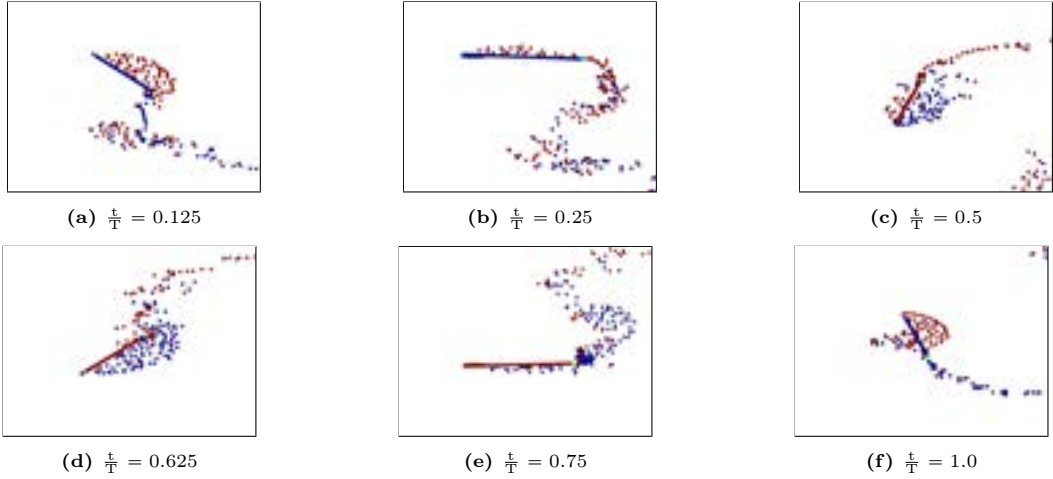


Figure 34: Visualization of the vortices shed from the leading and trailing edges by LDVM. The natural excitation of the FPG associated to $k = 0.628$ is shown.

10 Conclusion and Perspectives

An unsteady aeroelastic model of a Flapping Foil Power Generator (FFPG) has been developed using Deep Learning and LDVM. An active learning procedure allowed to converge on this aeroelastic model which has been further optimized with genetic algorithms (NSGA2). This study showed that both the aerodynamic effects associated to dynamic stall and the natural excitation of the system must be exploited to maximize the efficiency of such FFPG. One should understand from this study that semi-active Flapping Foil Power Generators are mainly driven by the reduced frequency k , the pitching amplitude θ_0 and by the stiffness K_h of the structure. A simple relation has been derived to optimize the aforementioned primary parameters to take advantage of the leading edge vortex that is developing on the foil undergoing significantly large pitching amplitudes. One could use the formula for the reduced frequency as a guideline for designing such FFPG. In order to exploit the natural excitation of the system, the stiffness can be easily determined by doing an analogy between this FFPG and a spring-mass system.

The LESP Discrete Vortex Method (LDVM) has been used to model the aerodynamic loads acting on the foil. The current work rely on this method which has some advantages but also some limitations. The primary source of uncertainty is the value set for the Leading Edge Suction Parameter (LESP). This macro-parameter depends on the Reynolds and the airfoil considered and it has been set according to the available values mentioned by the authors of LDVM. However, one should have understood that further investigations must be performed on this subject. More refined numerical simulations could be used to identify the LESP which corresponds to the current investigation.

Further investigations could also be conducted on the architecture used for the neural network and on its inputs vector. In fact, passing to the neural network a single input containing at the same time, parameters (x_f/c , etc.) and the states of the system (θ , h , etc.) might not be the best way to obtain accurate predictions. One could think about two different heads that would treat separately the system parameters and the states associated to the FFPG.

The authors would like to emphasize that the current work has considered only air for the fluid in which the FFPG would be operated. However, if one would like to think about a more realistic way of operating such system, considering a fluid with higher density may be more interesting. This idea is mainly motivated by the range of physical frequencies (Hz) encountered for a FFPG operated in air, which appears to be significantly high. Such high frequencies could be damageable for the structure of the system. Switching air for a fluid with higher density, may decrease the freestream velocity for a given Reynolds number. Given an optimal reduced frequency, this would lead to a decrease of the physical frequency encountered.

References

- [1] Office WET. Advantages and Challenges of Wind Energy;. Available from: <https://www.energy.gov/eere/wind/advantages-and-challenges-wind-energy>.
- [2] Office WPT. Benefits of Hydropower;. Available from: <https://www.energy.gov/eere/water/benefits-hydropower>.
- [3] Knoller R. Die Gesetze des Luftwiderstandes. Flug-und Motortechnik (Wien) 321. 1909.
- [4] John Young FBT, Lai JCS. BETZ ANALYSIS OF A SINGLE FLAPPING FOIL POWER GENERATOR. University of New South Wales, Canberra, Australia. 2016.
- [5] Katzmayer R. Effect of Periodic Changes of Angle of Attack on Behavior of Airfoils. TM No 147, NACA. 1922. Available from: https://digital.library.unt.edu/ark:/67531/metadc55795/m2/1/high_res_d/19930083152.pdf.
- [6] Hussein HMRWC A A. Stable, planar self propulsion using a hinged flap. IFAC-PapersOnLine 51(29), 395-399. 2018.
- [7] Kehoe MW. A historical overview of flight flutter testing. NASA Technical Memorandum 4720. 1995 09. Available from: <https://ntrs.nasa.gov/api/citations/19960004074/downloads/19960004074.pdf>.
- [8] Theodore T. General Theory of Aerodynamic Instability and the Mechanism of Flutter. TR No496, NACA. 1934.
- [9] Garrick IE. Propulsion of a flapping and oscillating airfoil. NACA Rept 567. 1937.
- [10] Mckinney W, Delaurier JD. Wingmill: An Oscillating-Wing Windmill. Journal of Energy. 1981;5:109-15. Available from: <https://api.semanticscholar.org/CorpusID:111041475>.
- [11] Coelho P. The Betz limit and the corresponding thermodynamic limit. Wind Engineering. 2023;47(2):491-6.
- [12] Jones K, Lindsey K, Platzer M. Numerical computation of flapping-wing propulsion and power extraction. 38th Aerospace Sciences Meeting and Exhibit. 1997.
- [13] Kinsey T, Dumas G. Parametric Study of an Oscillating Airfoil in Power Extraction Regime. Aiaa Journal - AIAA J. 2008 06;46:1318-30.
- [14] Zhu Q, Peng Z. Mode coupling and flow energy harvesting by a flapping foil. Physics of Fluids - PHYS FLUIDS. 2009 03;21.
- [15] Xiao Q, Liao W, Yang S, Peng Y. How motion trajectory affects energy extraction performance of a biomimic energy generator with an oscillating foil? Renewable Energy. 2012;37(1):61-75. Available from: <https://www.sciencedirect.com/science/article/pii/S0960148111002576>.
- [16] Ma P, Wang Y, Xie Y, Huo Z. Effects of time-varying freestream velocity on energy harvesting using an oscillating foil. Ocean Engineering. 2018;153:353-62. Available from: <https://www.sciencedirect.com/science/article/pii/S0029801818301379>.
- [17] Liu Z, Qu H, Shi H. Energy-harvesting performance of a coupled-pitching hydrofoil under the semi-passive mode. Applied Energy. 2020;267(C). Available from: <https://ideas.repec.org/a/eee/appene/v267y2020ics0306261920304013.html>.
- [18] Javed A, Djidjeli K, Xing JT. Low Reynolds Number Effect on Energy Extraction Performance of Semi-Passive Flapping Foil. Journal of Applied Fluid Mechanics. 2018 11;11:1613-27.
- [19] Peng Z, Zhu Q. Energy harvesting through flow-induced oscillations of a foil. Physics of Fluids - PHYS FLUIDS. 2009 12;21.
- [20] Boudreau M, Dumas G, Rahimpour M, Oshkai P. Experimental investigation of the energy extraction by a fully-passive flapping-foil hydrokinetic turbine prototype. Journal of Fluids and Structures. 2018;82:446-72. Available from: <https://www.sciencedirect.com/science/article/pii/S0889974618302287>.

- [21] Lucas MG. Energy Extraction from a Pitching-Plunging Airfoil. ISAE-SUPAERO, Université de Toulouse, 31055 Toulouse, FRANCE. 2022.
- [22] Hızlı H. Numerical and experimental investigation of pitching/plunging airfoils in hover. Middle East Technical University; 2012.
- [23] Jones K, Lindsey K, Platzer M. An Investigation of the fluid-structure interaction in an oscillating-wing micro-hydropower generator. *Advances in Fluid Mechanics*. 2003 01;36:73-82.
- [24] Gopalkrishnan R, Triantafyllou MS, Triantafyllou GS, Barrett D. Active vorticity control in a shear flow using a flapping foil. *Journal of Fluid Mechanics*. 1994;274:1â21.
- [25] Mumtaz Qadri MN, Shahzad A, Zhao F, Tang H. An Experimental Investigation of a Passively Flapping Foil in Energy Harvesting Mode. *Journal of Applied Fluid Mechanics*. 2019 09;12:1547-61.
- [26] Chorin AJ. Numerical study of slightly viscous flow. *Journal of fluid mechanics*. 1973;57(4):785-96.
- [27] Clarke N, Tutty O. Construction and validation of a discrete vortex method for the two-dimensional incompressible Navier-Stokes equations. *Computers & Fluids*. 1994;23(6):751-83.
- [28] Taylor I, Vezza M. Calculation of the flow field around a square section cylinder undergoing forced transverse oscillations using a discrete vortex method. *Journal of Wind Engineering and Industrial Aerodynamics*. 1999;82(1-3):271-91.
- [29] Ramesh K, Gopalarathnam A, Granlund K, Ol MV, Edwards JR. Discrete-vortex method with novel shedding criterion for unsteady aerofoil flows with intermittent leading-edge vortex shedding. *Journal of Fluid Mechanics*. 2014;751:500â538.
- [30] Åtomo S, Henne S, Mulleners K, Ramesh K. Unsteady lift on a high-amplitude pitching aerofoil. *Experiments in Fluids*. 2021 01;62.
- [31] Corban B, Bauerheim M, Jardin T. Discovering optimal flapping wing kinematics using active deep learning. *Journal of Fluid Mechanics*. 2023;974:A54.
- [32] Paszke A, Gross S, Massa F, Lerer A, Bradbury J, Chanan G, et al.. PyTorch: An Imperative Style, High-Performance Deep Learning Library; 2019. Available from: <https://arxiv.org/abs/1912.01703>.
- [33] Alguacil A, Bauerheim M, Jacob MC, Moreau S. Deep learning surrogate for the temporal propagation and scattering of acoustic waves. *AIAA Journal*. 2022;60(10):5890-906.
- [34] Message Passing Interface Forum. MPI: A Message-Passing Interface Standard Version 4.1; 2023. Available from: <https://www.mpi-forum.org/docs/mpi-4.1/mpi41-report.pdf>.
- [35] Pedregosa F, Varoquaux G, Gramfort A, Michel V, Thirion B, Grisel O, et al. Scikit-learn: Machine Learning in Python. *Journal of Machine Learning Research*. 2011;12:2825-30.
- [36] Blank J, Deb K. Pymoo: Multi-objective optimization in python. *Ieee access*. 2020;8:89497-509.
- [37] Avient. Carbon Fiber Composites;. Accessed: 2025-03-19. Available from: <https://www.avient.com/idea/carbon-fiber-composites>.
- [38] Virtanen P, Gommers R, Oliphant TE, Haberland M, Reddy T, Cournapeau D, et al. SciPy 1.0: Fundamental Algorithms for Scientific Computing in Python. *Nature Methods*. 2020;17:261-72.
- [39] Deb K, Pratap A, Agarwal S, Meyarivan T. A fast and elitist multiobjective genetic algorithm: NSGA-II. *IEEE transactions on evolutionary computation*. 2002;6(2):182-97.
- [40] Krügener M, Zapata Usandivaras J, Bauerheim M, Urbano A. Coaxial-injector surrogate modeling based on Reynolds-averaged Navier–Stokes simulations using deep learning. *Journal of Propulsion and Power*. 2022;38(5):783-98.
- [41] Dask Development Team. Dask: Library for dynamic task scheduling; 2016. Available from: <http://dask.pydata.org>.

- [42] Corke TC, Thomas FO. Dynamic stall in pitching airfoils: aerodynamic damping and compressibility effects. *Annual Review of Fluid Mechanics*. 2015;47(1):479-505.
- [43] Green R, Galbraith RM, Niven A. Measurements of the dynamic stall vortex convection speed. *The Aeronautical Journal*. 1992;96(958):319-25.